




University of
Stavanger

FACULTY OF SCIENCE AND TECHNOLOGY

MASTER'S THESIS

Study program/specialization: Petroleum Engineering/Natural Gas Engineering	Spring 2019 Open
Author: Vladislav Volkov	 (signature of author)
Supervisor: Professor Zhixin Yu	
Title of master's thesis: Aqueous Electrochemical Reduction of Carbon Dioxide using Carbon Supported Copper Electrocatalyst	
Credits (ECTS): 30	
Key words: Carbon dioxide Electrochemical reduction Catalysts Copper Nanoporous carbon materials	Number of pages: 46 Stavanger, 10/07/2019

Acknowledgements

I would like to thank my supervisor Professor Zhixin Yu for providing with the opportunities for conducting this work and guidance all the way through it. Additional gratitude shall be mentioned for the endless positive attitude and inspiring courses during Natural Gas Engineering M.Sc. program.

Special thanks to the Department of Energy and Petroleum Technology of University of Stavanger in the person of the Head of Department, Øystein Arild, for the financial support of the academic journey to the School of Materials Science and Engineering at Tianjin University of Technology. Most of the investigations of this thesis were performed at the Institute of New Energy Materials and Low-Carbon Technologies, and thus I want to express appreciation to Institute's Deputy Director – Professor Yi Ding, Professors Zhao and Zhang, Mrs. Wang Jian and master students, for their valuable collaboration and true warm welcome.

I want to thank members of Catalysis group at University of Stavanger: Dr. Kalai and Ph.D. candidates Huong Lan Huynh and Kristian Stangeland for their wise advises, example of the efficient work performance, knowledge-sharing and help with academic tasks. Special appreciation to Kristian Stangeland for his contribution to this work.

I am deeply grateful to all university staff and my classmates for these memorable years at University of Stavanger.

Abstract

The atmospheric concentration of CO₂ has been rising progressively from 280 parts per million (ppm) in the pre-industrial time to 410 ppm in 2018. The anthropogenic CO₂ emissions are dominated by fossil fuel sources, which has led to increasing interest in carbon capture and storage and CO₂ utilization technologies. One approach for CO₂ utilization is the electrochemical reduction of CO₂. Advantages of electrochemical reduction of CO₂ include the modular and compact design that allows for easy scale-up, generates low amounts of waste, and the process is easily controlled. However, a key challenge for developing viable CO₂ reduction processes is the discovery of affordable, efficient, selective, and stable catalysts.

Copper is an interesting metal for electrochemical reduction of CO₂ because it can produce a range of different products such as hydrocarbons, alcohols, formate, and carbon monoxide. The challenge is to find suitable modifiers that can improve the selectivity towards the desired product. Carbon supported metallic nanoparticles has emerged as a promising candidate for electrochemical reduction of CO₂. So far, only a few works have investigated the carbon supported Cu nanoparticles. These studies have found that the selectivity and the faradaic efficiency of Cu can be improved by the carbon support.

In this thesis, the activities of Cu nanoparticles supported on different multi-walled carbon nanotubes (MWCNT1020 and MWCNT2040) and Ketjenblack (KB) toward electrochemical reduction of CO₂ with emphasis on formic acid and methanol production. The catalysts were prepared by the homogeneous deposition precipitation method and characterized by thermal gravimetry, X-ray diffraction, scanning electron microscopy, Raman spectroscopy, and X-ray photoelectric spectroscopy. The faradaic efficiency was highest for H₂, followed by HCOOH. The activity of MWCNT supported Cu (Cu = 5, 10, and 20 wt. %) with different loading showed that the highest faradaic efficiency was obtained at 20 wt. %. Furthermore, only small changes in product selectivity were observed. Comparing two different MWCNTs and KB showed that the support could have an impact on the product selectivity. It was found that the MWCNT1020 had a higher oxygen content than the other carbon supports and generated a significant amount of methanol. Moreover, the MWCNT1020 supported Cu catalyst achieved the highest total faradaic efficiency. The results suggest that the carbon support can play a significant role in catalytic performance for electrochemical reduction of CO₂ to formic acid and methanol.

Table of Contents

Acknowledgements.....	i
Abstract.....	ii
List of Figures.....	v
List of Tables.....	v
1 Introduction.....	1
1.1 Background.....	1
1.2 Scope of present work.....	3
2 Literature review.....	4
2.1 Electrochemistry and typical electrolytic cell compartments.....	4
2.1.1 Working electrode (WE) and overpotential.....	5
2.1.2 Reference electrode (RE) and counter electrode (CE).....	6
2.2 Review of electrochemical catalysts for the reduction of CO ₂	7
2.2.1 Overview of electrodes for CO ₂ RR.....	7
2.2.2 Cu electrodes for CO ₂ RR.....	9
2.2.3 Cu modified catalysts for CO ₂ RR.....	11
2.2.4 Supported Cu-based catalysts.....	12
2.3 Catalyst preparation by homogeneous deposition precipitation (HDP).....	13
3 Experimental.....	16
3.1 Materials and equipment.....	16
3.2 Electrode fabrication.....	17
3.2.1 Catalyst synthesis.....	17
3.2.2 Catalyst ink preparation.....	19
3.3 Catalyst characterization procedures.....	19
3.4 Activity tests.....	21
3.4.1 Cyclic voltammetry.....	21
3.4.2 Chronoamperometry.....	21
3.5 Analytical chemistry techniques.....	21
3.5.1 Gas Chromatography.....	22
3.5.2 Nuclear Magnetic Resonance (NMR).....	22
4 Results and discussion.....	24
4.1 Catalyst characterization.....	24
4.1.1 Thermal gravimetric analysis.....	24
4.1.2 SEM analysis.....	25
4.1.3 X-ray diffraction.....	25

4.1.4	Raman spectroscopy	27
4.1.5	X-ray photoelectron spectroscopy	28
4.2	Evaluation of catalysts for ECR of CO ₂	29
4.2.1	Cyclic voltammetry.....	29
4.2.2	Chronoamperometry	32
5	Conclusions and future work	35
5.1	Conclusion.....	35
5.2	Recommendations for future work	35
	References.....	37
	Appendix A.....	40
	Appendix B.....	41

List of Figures

Figure 1.1. A chart demonstrating the increasing concentrations of carbon dioxide in the atmosphere (in parts per million) observed at NOAA's Mauna Loa Observatory [1] over the course of 60 years.	1
Figure 2.1. A typical three-electrode electrolytic cell [22].	5
Figure 2.2. Experimentally [19] determined current and product distribution as a function of applied potential vs RHE in CO ₂ RR at a Cu electrode (reaction conditions: 0.1M KHCO ₃ (PH 6.8) at 18.5 °C).	10
Figure 4.1. TGA curves of calcined materials in a flow of air.	24
Figure 4.2. SEM images of the calcined (a) and reduced (b) 20Cu/MWCNT1020 catalyst. ...	25
Figure 4.3. XRD patterns of Cu supported on different carbon materials after HDP (a), calcined (b) and reduced (c).	26
Figure 4.4. Raman spectra over calcined and reduced 20%Cu/MWCNT2040.	27
Figure 4.5 XPS spectra of reduced and calcined 20Cu/MWCNT2040 and reduced 20Cu/MWCNT1020 (a) Cu _{2p} , (b) C1s, (c) O1s, and (d) survey spectra.	28
Figure 4.6. (a) CV profiles for blank CP versus modified CP with 20Cu/MWCNT2040 as WE in CO ₂ saturated electrolyte and (b) current profiles obtained at a fixed potential of -0.88 V for 4500 s.	30
Figure 4.7. Cyclic voltammetry profiles for 1 cm ² catalysed carbon cloth with 2 mg of (a) 20Cu/KB, (b) 20Cu/MWCNT1020, (c) 20Cu/MWCNT2040, (d) 10Cu/MWCNT2040, and (e) 5Cu/MWCNT2040 0.5M KHCO ₃ electrolytes purged with N ₂ and CO ₂ gases.	31
Figure 4.8. Chronoamperograms of 150 min electrolysis at -0.877 V vs. RHE using 5 different WEs in a CO ₂ saturated 0.1 M KHCO ₃ electrolyte with 5 mL.min ⁻¹ CO ₂ flow.	32
Figure 4.9. Faradaic efficiencies of identified products for carbon-supported Cu catalysts after 9000 s held at -0.88 V.	33
Figure 4.10. Chronoamperometric curves at potentials of -0.5 to -1.2 V vs RHE for 9000 s in CO ₂ saturated KHCO ₃ electrolyte over 20Cu/MWCNT1020.	33
Figure 4.11. Faradaic efficiency for generation of H ₂ , CO, HCOOH and CH ₃ OH over 20Cu/MWCNT1020 after 9000 s long electrolysis sets at different potentials.	34

List of Tables

Table 2-1. Standard potentials of CO ₂ in aqueous solutions (V vs. SHE) at 1.0 atm and 25 °C calculated according to the standard Gibbs energies of the reactants in the reactions [22].	7
Table 3-1. Summary of chemicals used for catalyst synthesis and catalytic testing.	16
Table 3-2. Summary of equipment used for catalyst synthesis and catalytic testing.	17
Table 3-3. Main characteristics of MWCNTs and Ketjenblack supports [28; 43].	17
Table 3-4. Denotations of the synthesised catalysts.	18
Table 4-1. TGA curves in a flow of air of calcined samples.	24
Table 4-2. Summary of surface composition and distribution of carbon and oxygen species.	29

1 Introduction

1.1 Background

The drastic social changes and technological achievements during the 20th century has imposed a great number of challenges that humanity is facing today. Earth's population have increased [38] from approximately 2.5 billion in 1950 to 7.7 billion in 2019 and is expecting to reach 9 billion by 2050. In addition to population growth, humankind tends to improve the quality of living, demanding higher energy consumption. The resulting increase in fossil fuels consumption has led to rising levels of atmospheric carbon dioxide (CO₂) ever since the Industrial Revolution in the 1850s. Figure 1 shows the atmospheric concentration of CO₂ over the last 60 years [1]. The CO₂ levels has been rising progressively from 280 parts per million (ppm) in the pre-industrial level – to the level of 410 ppm in 2018.

The present atmospheric concentration of carbon dioxide exceeds the threshold safety value of 350 ppm [36]. The fuel sources contributing to carbon dioxide emissions vary significantly by region and industry sector, but coal and petrochemicals significantly dominate on a global scale [2]. Climate reports released nowadays state evidence for long-term climate changes due to emissions of greenhouse gases (GHGs), which has resulted in a global effort in lowering GHG emissions [37].

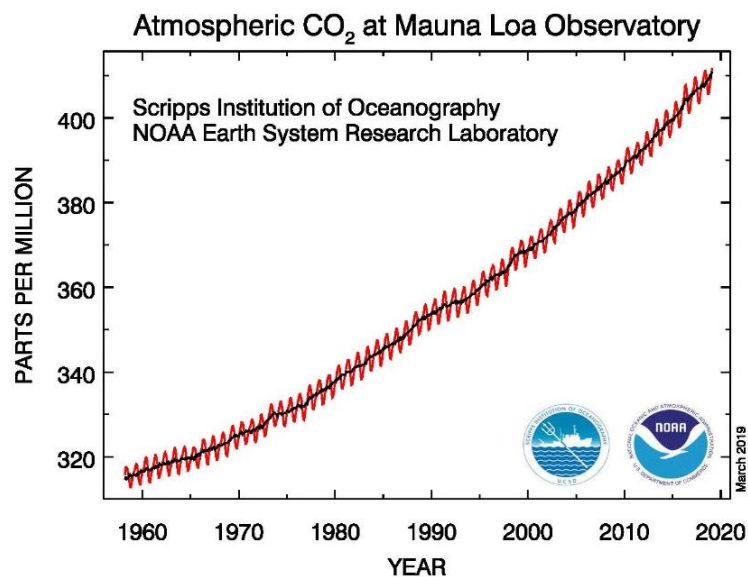


Figure 1.1. A chart demonstrating the increasing concentrations of carbon dioxide in the atmosphere (in parts per million) observed at NOAA's Mauna Loa Observatory [1] over the course of 60 years.

The desire to decrease CO₂ emissions has driven the research towards finding alternative technologies. One favourable strategy introduced in recent years is the adoption of carbon capture and storage (CCS) and carbon capture and utilization (CCU) technologies. Carbon capture technologies offer routes for direct capture of volumes of CO₂ gas from the atmosphere or technologies that prevent CO₂ emissions to the surroundings from colossal emitters. The main advantage of CCU is that it may provide an economic advantage as CO₂ is converted into valuable products.

Several catalytic processes have been investigated for CO₂ conversion, including thermochemical, photochemical, biological, and electrochemical processes. A wide range of products can be produced through CO₂ hydrogenation in these processes, such as CO, hydrocarbons, oxygenates (i.e. alcohols, formic acid, etc.), and other organic compounds. Hence, these routes offer an alternative method to fossil sources for producing fuels and chemicals. It is likely that a combined effort of several of these processes is needed to meet the energy demand and alleviate the impact on climate change.

The conversion of CO₂ using electrocatalysis approaches has recently attracted considerable attention due to several advantages [23]. Firstly, the process is easily controllable by electrode potentials and reaction temperature. The electricity used to drive the process can be obtained from renewable sources (i.e. solar, wind, hydropower, geothermal). The electrochemical reaction systems are also compact, modular and easy for scale-up applications. Lastly, the supporting electrolytes can be fully recycled so that the overall chemical consumption can be minimized to only water or wastewater. However, CO₂ reduction reaction (CO₂RR) have large kinetic barriers that must be overcome. A key challenge for large scale utilization of electrochemical processes is, therefore, the development of affordable, efficient, selective, and stable catalysts.

Carbon supported metallic nanoparticles has emerged as a promising candidate for ECR of CO₂ [5; 12; 20; 32; 48] . There has only been a limited amount of studies that have explored these catalysts so far for electrochemical CO₂RR. The results from these works indicate that higher stability as well as enhanced activity can be achieved compared to Cu electrodes and Cu nanoparticles. However, there are still many questions that need to be answered due to the complexity of CO₂RR on Cu-based materials. Cu-based materials can simultaneously produce a range of different gas and liquid phase products, such as CO, hydrocarbons, and oxygenates. This work focuses on Cu supported on carbon materials for the ECR of CO₂.

1.2 Scope of present work

In this study, a series of carbon supported Cu catalysts were prepared by the homogeneous deposition precipitation method. The catalysts were characterized by means of thermal gravimetry, X-ray diffraction, scanning electron microscopy, Raman spectroscopy, and X-ray photoelectron spectroscopy. The catalysts were tested for electrochemical reduction of CO₂ by cyclic voltammetry and chronoamperometry in aqueous solution of potassium hydrogen carbonate. The emphasis in this work was on promoting the generation of formic acid and methanol. The goal of the study was to:

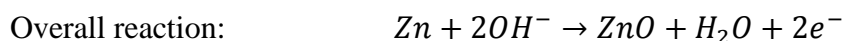
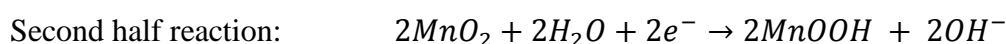
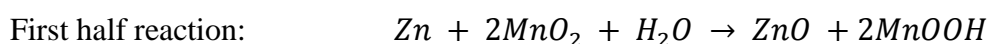
- Determine the effect of Cu loading on the selectivity of carbon supported Cu catalysts
- Investigate the effect of different carbon supports and identify their contribution to selectivity and faradaic efficiency

2 Literature review

2.1 Electrochemistry and typical electrolytic cell compartments

Electrochemistry is the branch of physical chemistry that is concerned with the interrelation of electrical and chemical effects in the system caused by the passage of an electric current through it to drive an otherwise non-spontaneous chemical reaction [4]. Thus, electrochemical processes involve oxidation-reduction reactions, where electrons e^- transferred to or from a molecule or ion changing its oxidation state. The aforementioned reactions may occur due to the application of external voltage to a system or its esoteric release of chemical energy.

As an example, metallic copper plates, used in architecture for roofing, participate with carbon dioxide from milieu in redox reactions leading to the formation of basic carbonates on its surface, known as patina: $2Cu + CO_2 + O_2 + H_2O \rightarrow Cu_2(OH)_2CO_3$. Its colour ranges from matte sandstone yellow to deep blue and green. Considering electrochemistry, we usually think of reactions in terms of half-cell reactions, representing clearly work done by electrons. Electrochemistry happens for electricity production inside alkaline batteries – galvanic cells, where zinc (Zn) anode reacts with manganese dioxide (MnO_2) cathode, while potassium hydroxide serves as a source of water and hydroxide ions or alkaline compound. As a result, manganese dioxide cathode is reduced and the zinc anode becomes oxidized. Electrons are released during the oxidation of zinc atom and these free electrons are utilized to provide devices with power.



Essentially the opposite of a galvanic cell, an electrolytic cell performs electrolysis, which uses electricity, electro-, to do the breaking apart, -lysis. Seawater electrolysis is one of the electrolysis technologies that uses electrical current to split water into hydrogen and oxygen gas. Although it is debatable when it was first discovered, the water electrolysis has been intensively studied since the initial breakthroughs during the late 18th century and early 19th century. Chemical systems are studied by the means of electrochemical measurements for a variety of reasons including a goal of obtaining a thermodynamic data of a specific reaction or generation of an unstable intermediate and studying its rate of decay. Understanding of fundamental principles of electrode reactions together with electrical properties of electrode-solution interfaces is crucial for the application of electrochemical methods [4].

A typical H-type electrolytic cell consists of a working electrode (WE), a counter electrode (CE) and a reference electrode (RE) attached in a circuit to an electrochemical instrument is illustrated on a figure 2.1.

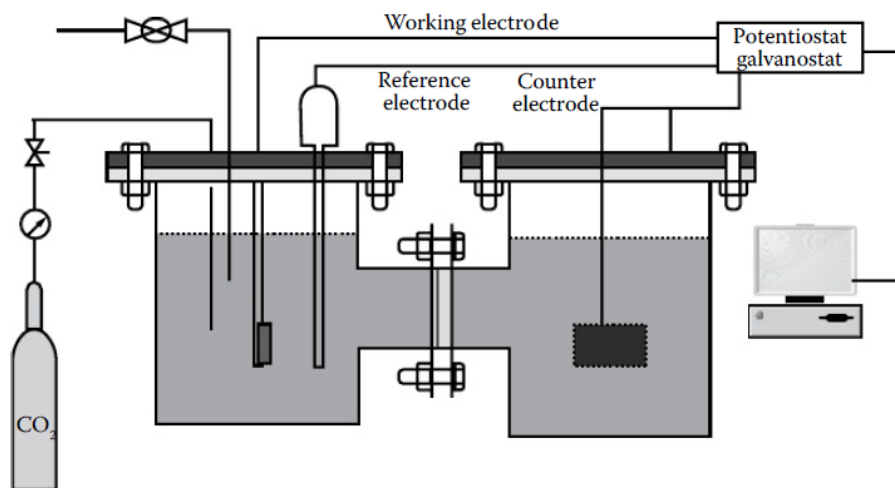


Figure 2.1. A typical three-electrode electrolytic cell [22].

2.1.1 Working electrode (WE) and overpotential

The actual electrochemical step can be accompanied by different chemical reactions, either in bulk or on the electrode surface. Electron transfer at the electrode surface depends upon the electrode potential. The transition in electric potential crossing from one conducting phase to another usually occurs almost entirely at the interface. The sharpness of the transition implies that an electric field exists at the interface, and one can expect it to exert effects on the behaviour of charge carriers (electrons or ions) in the interfacial region. The magnitude of the potential difference at an interface affects the relative energies of the carriers in two phases; hence, it controls the direction and the rate of charge transfer. Thus, the measurement and control of cell potential are one of the most important aspects of experimental electrochemistry. The cell potential, measured in volts V, $1 \text{ V} = \text{one joule/coulomb J/C}$, is a measure of the energy available to drive charge externally between the electrodes. When a potential difference is applied to a WE, the goal is to utilise all the applied energy to create a potential energy drop between the WE surface and the solution.

Overpotential is the amount of non-reversible energy required to overcome the energy barrier of a reaction, and it reveals how far the electrode is from its equilibrium potential upon a passage of Faradaic current [22]. This deviation is termed electrode polarization and overpotential determines the extent of polarization, $\eta = E_{0_{redox}} - E$, where $E_{0_{redox}}$ is the

standard thermodynamic redox potential, and E is the onset potential at which the redox reaction is experimentally observed [31]. The overpotential is thus different from the “driving force” of the reaction defined as the opposite of the standard free energy of the reaction: $\Delta G^\circ = \pm F(E - E^\circ)$, referred to the standard state of the reactant and product system [41].

2.1.2 Reference electrode (RE) and counter electrode (CE)

Counter or auxiliary electrode, usually a Pt surface, provides a circuit over which current is either applied. It establishes the electrical potential against which potentials at other electrodes may be measured. In electrolytic cell, the auxiliary is isolated from the working electrode. Reactions at reference electrodes are half-cell reactions that are isolated in their own chamber and utilized to complete the circuit providing a benchmark of voltage in a cell. The ultimate RE is Normal Hydrogen Electrode (NHE) – reduction of hydrogen ions to hydrogen gas at the electrode. This means that hydrogen gas is bubbled at 1 atm across a Pt plate in an acid solution. Since the potential of a single electrode cannot be measured, it is merely assigned to zero 0 V by definition:



Bubbling of hydrogen at one standard atmosphere through the solution represents some safety issues, therefore, alternative REs are used. One of the most experimentally utilized REs is Ag/AgCl saturated KCl reference electrode, based on the reduction of silver chloride to metallic silver: $AgCl(s) + e^- \rightarrow Ag(s) + Cl_{aq}^-$.

Both oxidised and reduced forms are at the wire surface, and since chloride is a product [53], it shows up in the Nernst equation for this half-cell, producing a reference potential of 0.197 V. Employing this and the pH value of an aqueous solution, experimentally obtained voltage may be converted to NHE and RHE by following equations [53], respectively.

$$E(\text{NHE}) = E(\text{Ag}/\text{AgCl}) + 0.197 \text{ V} \quad (2.2)$$

$$E(\text{RHE}) = E(\text{NHE}) + 0.0591 \cdot \text{pH} \quad (2.3)$$

In addition, besides minimizing required energy barrier for the activation of carbon dioxide molecules, an efficient electrocatalyst should selectively accelerate reduction at feasibly low overpotentials with sufficient current densities [31]. Faradaic efficiency (FE) and current density are usually utilized in order to compare different catalysts and evaluate their catalytic efficiency. Current density, expressed in amperes per square meters ($\text{A}\cdot\text{m}^{-2}$), is the amount of charge per unit time that travels through unit cross section of a conductor [21], and it is calculated by dividing the generated electric current with the geometric surface area of a

working electrode or its electrochemical active surface area [31]. FE of a specific product of a CO₂ electroreduction process defines the charge (electrons) efficiency in an electrochemical reduction reaction. Thus, its magnitude calculation involves the number of electrons consumed during reaction and it can be affected by chemical composition, morphology of an electrocatalyst and reaction conditions during electrolysis process.

2.2 Review of electrochemical catalysts for the reduction of CO₂

2.2.1 Overview of electrodes for CO₂RR

Synthesis of chemicals/hydrocarbons from carbon dioxide is a complex multistep reaction with adsorbed intermediates that can proceed through two-, four-, six-, and eight-electron reduction pathways in gaseous, aqueous, and non-aqueous phases at both low and high temperatures, resulting in various reduction products. Thus, cathodic reduction of carbon dioxide may undergo through several possible pathways, and they are normally accompanied by hydrogen evolution reaction (HER). The reaction pathways and resulting product distributions depend on the electrocatalyst property, proton availability, identity of electrolyte, applied cathode potential, carbon dioxide concentration, mass transport, pH, and temperature [22]. The thermodynamic electrochemical half-reactions of CO₂ reduction and their associated standard electrode potentials are summarised in a Table 2-1.

Table 2-1. Standard potentials of CO₂ in aqueous solutions (V vs. SHE) at 1.0 atm and 25 °C calculated according to the standard Gibbs energies of the reactants in the reactions [22].

Electrochemical Thermodynamic Half – Reactions	Electrode Potentials (V vs. SHE) at Standard Conditions
$CO_2(g) + 2H^+ + 2e^- = HCOOH(l)$	-0.250
$CO_2(g) + 2H_2O(l) + 2e^- = HCOO^-(aq.) + OH^-$	-1.078
$CO_2(g) + 2H^+ + 2e^- = CO(g) + H_2O(l)$	-0.106
$CO_2(g) + 2H_2O(l) + 2e^- = CO(g) + 2OH^-$	-0.934
$CO_2(g) + 6H^+ + 6e^- = CH_3OH(l) + H_2O(l)$	+0.016
$CO_2(g) + 5H_2O(l) + 6e^- = CH_3OH(l) + 6OH^-$	-0.812
$CO_2(g) + 8H^+ + 8e^- = CH_4(g) + 2H_2O(l)$	+0.169
$CO_2(g) + 6H_2O(l) + 8e^- = CH_4(g) + 8OH^-$	-0.659
$2CO_2(g) + 2e^- = C_2O_4^{2-}(aq.)$	-0.590
$2CO_2(g) + 12H^+ + 12e^- = CH_2CH_2(g) + 4H_2O(l)$	+0.064
$2CO_2(g) + 8H_2O(l) + 12e^- = CH_2CH_2(g) + 12OH^-$	-0.764
$2CO_2(g) + 12H^+ + 12e^- = CH_3CH_2OH(l) + 3H_2O(l)$	+0.084
$2CO_2(g) + 9H_2O(l) + 12e^- = CH_3CH_2OH(l) + 12OH^-$	+0.744

Currently, excess voltage beyond what is thermodynamically required is needed to achieve sufficient activity. This excess voltage is referred to as the overpotential and lowering the overpotential through the discovery of more active catalysts increases the energy efficiency of producing chemicals and fuels electrochemically through CO₂ reduction [25]. The CO₂RR process on a catalyst surface consists of three main steps: (1) the first step of CO₂RR is the chemical adsorption of CO₂ and interaction with atoms on the catalyst surface; (2) CO₂ activation and reduction via catalyst-initiated electron/proton transfers; (3) and product desorption and recovery of the catalyst surface for next round of reaction [24]. Generally, transferring one electron to CO₂ to generate *CO₂^{•-} is believed to be the rate-determining step. This is because of the high energy barrier required to initiate this process on most transition metal-based catalysts. It has also been observed that the reactivity of *CO₂^{•-} is a key factor that governs the distribution of final products [47]. Hence, the stabilization of the aforementioned high-energy intermediate could be key to achieve high reaction rates and an efficient CO₂ reduction process [27]. It has been reported by several groups that a -1.9 V vs. NHE is needed for the one-electron reduction to CO₂^{•-}, while a more positive potential is required for multielectron charge transfer.

The mechanism for the electrochemical reduction (ECR) of CO₂ has been studied experimentally and theoretically over the past decades to understand the kinetic reaction pathways for different products and the factors governing the selectivity of products over different metal electrodes. Four groups of metallic electrodes can be distinguished based on their primary product during ECR of CO₂ in aqueous supporting electrolytes [23], [27]:

1. In, Sn, Hg, Cd, Bi, Tl, and Pb are mainly selective to produce formic acid and formate, the simplest carboxylate anion – product of deprotonation of formic acid.
2. Zn, Au, Pd, Ga, and Ag produce carbon monoxide as a major product.
3. Cu exhibits high electrocatalytic activity towards the formation of a wide range of hydrocarbons and oxygenates, and aldehydes besides CO and formate.
4. Ni, Fe, Al, Pt, and Group VIII elements (except Pd) show low electrocatalytic activity towards CO₂ECR and catalyse mostly the HER under ambient conditions.

The mechanistic pathway on Group 1 electrodes, where formate is the major product, has been speculated to proceed via a weakly adsorbed CO₂^{•-} radical anion that reacts with water to form formate. The intermediate is expected to bind to the catalyst through one of the oxygen atoms, thus, making the carbon atom available for hydrogenation. High overpotential is required to

achieve reasonable selectivity towards formate, because the redox potential for the formation of the $\text{CO}_2^{\bullet-}$ intermediate is -1.90 V versus standard hydrogen electrode (SHE) [27].

Metals of Group 2 and Group 3 bind CO_2 via Carbon atom in adsorbed carboxyl intermediate ($^*\text{COOH}$, where * denotes an adsorbed species), which is assumed to be formed through a proton–electron transfer to CO_2 molecule. The carboxyl intermediate will react with the second electron/proton to form the $^*\text{CO}$ intermediate and water. Both experimental and theoretical reports have suggested that the binding energy of $^*\text{CO}$ on metal surfaces influences the overall activity and selectivity of the ECR to produce CO, hydrocarbons, and oxygenates. However, experimental literature indicates that the formation of $^*\text{COOH}$ happens also via the formation of a $\text{CO}_2^{\bullet-}$ radical anion.

For production of hydrocarbons and oxygenates, a catalyst should bind CO strongly enough to limit the desorption of CO from the surface and, thereby, facilitate further reduction to the desired products. Too strongly bound CO may poison the catalyst surface, for example, in the case of Pt and Fe in Group 4. Optimum CO binding is required for a catalyst, such as Cu, to proceed to further protonation (formation of $^*\text{HCO}$ or $^*\text{COH}$) to form multi-carbon products via a series of complicated proton and electron transfer reactions. However, it is a great challenge to optimize the binding energy of each intermediate individually. The binding energies of $^*\text{COOH}$, $^*\text{CO}$ and $^*\text{CHO}$ are typically correlated through the “scaling relations”, i.e. the binding energy of $^*\text{CO}$ is positively correlated to that of $^*\text{COOH}$ and $^*\text{CHO}$, making it difficult to control them independently [27]. Recently, Kuhl et al. [26] showed that Group 2 metal electrodes also can produce methane or methanol, but they require a higher potential than Group 3 and Group 4 metals. Furthermore, investigations by spectroscopic techniques as well as density functional theory (DFT) and theoretical modelling have suggested that there is a higher surface coverage of adsorbed CO on these metal electrodes. This implies that the reduction of adsorbed CO is the rate-determining step.

2.2.2 Cu electrodes for CO_2RR

Cu has been found to be unique among the metal electrodes due to its ability to produce a high quantity of hydrocarbons in CO_2RR , which makes copper cathodes among the most promising options for producing hydrocarbon by electrochemical reduction. The aqueous reduction of CO_2 to hydrocarbons at copper electrodes was first reported in literature in 1985 by Hori et al. [19]. They found that the product distribution over Cu electrodes depended on the applied potential. Figure 2.1 shows the current and product distribution determined experimentally

over the Cu electrode. At low negative potentials, the Cu electrode produced a mixture of H₂, HCOOH, and CO. On the other hand, methane and ethylene was the dominant products at high negative potentials. A potential of +0.17 V vs. RHE is sufficient for reducing CO₂ to methane based on thermodynamics. However, potentials of approximately -0.8 V have been determined experimentally for the onset of CH₄ production from CO₂ [35]. It is interesting that methanol is not among the products, as Cu-based catalysts are highly efficient methanol synthesis catalysts [45].

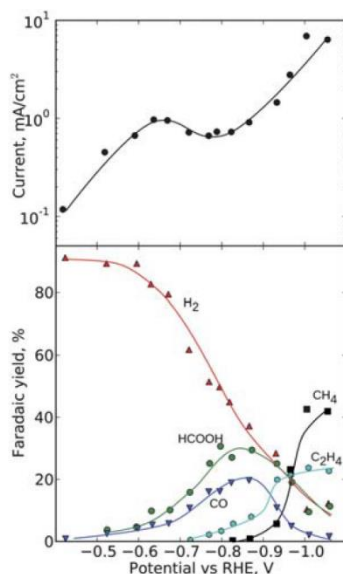


Figure 2.2. Experimentally [19] determined current and product distribution as a function of applied potential vs RHE in CO₂RR at a Cu electrode (reaction conditions: 0.1M KHCO₃ (PH 6.8) at 18.5 °C).

Hydrogenation of carbon dioxide to methanol is slightly exergonic ($\Delta G^0 = -4.1$ Kcal.Mol⁻¹), and to methane to a greater extent ($\Delta G^0 = -1.3$ Kcal.Mol⁻¹), because of the favourable thermodynamics of water formation [23]. Moreover, potentials required for the formation of C=O containing products are larger than those for the production of C-H and C-OH compounds [47]. DFT (density functional theory) calculations based on computational hydrogen electrode (CHE) model suggest that protonation of CO* to CHO* is the key potential-limiting step for the formation of hydrocarbons on Cu surfaces [47]. The proposed lowest energy pathways to CH₄ is believed to follow the order of CO₂ → *COOH → *CO → *CHO → *CH₂O → *CH₃O → CH₄ + *O → CH₄ + *OH → CH₄ + H₂O.

The formation of ethylene requires the controlled coupling between CHO* and CH₂O* into *OCHCHO*, *OCHCH₂O* or *OCH₂CH₂O*, followed by further hydrogenation/dehydration

reactions. Recent advance in computation further reveals that the formation of *COH or *CHO intermediate during the hydrogenation of *CO can also be key to determining the preferred products (CH₄, C₂H₄, and CH₃OH) on a Cu (111) facet [47]. Peterson et al. [35] suggested that the formation of CH₄ and CH₃OH is related to the protonation of methoxy. Protons in the solution that directly react with the methyl end of the methoxy would result in methane formation. On the other hand, protons transferred from the metal surface to the methoxy would result in methanol formation.

Significant deactivation of Cu electrodes with regard to the hydrocarbons formation occurs during CO₂RR [18]. The deactivation of Cu electrode typically is quite rapid, and the features of the deactivation of Cu electrode depend on the reagent used for the electrolyte solution. During long term electrolysis, the deactivation can be suppressed if the electrolyte solution is appropriately purified.

2.2.3 Cu modified catalysts for CO₂RR

Compared to bulk Cu films or powders, nanoparticles possess a higher surface area to volume ratio and consequently, may be more active for CO₂RR. Zhu et al. [51] investigated continuous hydrothermal synthesis production of Cu₂O nanomaterials for ECR of CO₂ in 0.5 M KHCO₃ solution using a rotating ring-disc electrode (RRDE). They showed that exclusive production of formate could be obtained with a maximum Faradaic efficiency of 66% at 0.8 V vs RHE. Ohaya et al. [33] studied ECR of CO₂ on CuO/Zn and Cu₂O/Zn powder-pressed mixtures as electrodes in KOH/methanol solution. Only CO and formic acid were detected over the Zn powder-pressed electrodes. It was found that Cu₂O/Zn was significantly more active than CuO/Zn, which achieved methane and ethylene efficiencies of 7.5 and 6.8%, respectively.

Griffing et al. [15] examined Cu₂O nanoparticles supported on glassy carbon electrode for CO₂RR in a two-compartment electrochemical cell in KHCO₃ electrolyte under flowing CO₂. They found that the main gas phase products were CO, H₂, CH₄, and C₂H₄, while C₂H₅OH and C₃H₅OH were detected in the liquid phase. These results are in agreement with previous reports on Cu₂O deposited on carbon fiber paper supports as well as Cu₂O catalysts prepared by electrodeposition or thermal oxidation techniques. The Cu₂O phase underwent partial reduction during experiments and it was suggested that the Cu⁺/Cu⁰ ratio influenced the product selectivity. Loiudice et al. [29] prepared Cu nanocrystalline spheres and cubes of different sizes. A higher selectivity for ethylene was obtained for Cu cubes. Furthermore, a size-dependent selectivity was observed where the highest selectivity for C₂ products was obtained

for 44 nm Cu cubes. Chang et al. [7] investigated Cu₂O supported on a carbon cloth in a three-compartment cell with 0.5 M NaOH electrolyte. The catalyst achieved a mass activity of 0.94 mA/mg, where the predominant product was methanol.

2.2.4 Supported Cu-based catalysts

The interaction between different components in supported catalysts has been shown to result in interfacial active sites with synergistic effects that can enhance the catalytic performance. These effects are widely recognized in heterogeneous catalysis and have recently also been studied for ECR of CO₂ [18]. For example, Kenis et al. [30] found that TiO₂ could stabilize the CO₂^{•-} intermediate and thereby enhance the reduction of CO₂ to CO by Ag NPs.

Pérez-Cadenas et al. [34] demonstrated that xerogels supported Cu nanoparticles of 50-100 nm were able to convert CO₂ to C₁–C₃ paraffins and olefins at –1.65 V versus Ag/AgCl. The xerogel supported Cu nanoparticles displayed a broader product distribution compared to electropolished Cu foil. Furthermore, carbon supported metal particles have also been shown to enhance the performance of ECR [39].

Carbon nanomaterials are widely recognized as catalyst support materials due to their tunable special physiochemical characteristic, controllable textures and microstructures, mechanical strength and electrical conductivity. In some cases, carbon-based supports are preferred over alumina and silica supports owing to higher thermal stability, higher surface area, resistance to corrosion in acidic and basic medium and ease in the recovery of precious metal particles [13]. It has been reported that the activity of the catalyst increases during liquid phase hydrogenation reactions for carbon supported catalysts compared to alumina supported ones. The potential use of nanoporous carbon materials as electrocatalysts for the CO₂RR is due to the chemical diversity on the surface and porous structures of NPC [10]. When the porous carbon materials are reacted with an oxidizing agent, i.e. nitric acid, oxygen-containing groups are formed at the surface of the support [44]. HNO₃ is commonly utilized as the oxidizing agent, which incorporates oxygen containing chemical groups to the surface (CHO, CO, OH, and COOH). Furthermore, these oxygen-containing surface groups can also act as anchoring sites for the catalyst particles [40]. Other surface species can also be introduced to the carbon materials to achieve different effects, such as nitrogen doping [49].

There have been a few reports of Cu supported on porous carbon materials for ECR of CO₂. Yamamoto et al. [48] studied different metals supported on activated carbon fiber for CO₂ECR to syngas. The supported catalysts showed higher current density and selectivity compared to

the planar electrodes. Hossain et al. [20] prepared carbon nanotubes (CNTs) supported Cu catalysts for ECR of CO₂. The highest activity obtained at 20 wt.% Cu loading for the predominant formation of methanol with a faradaic efficiency of approximately 38.5%. This was suggested to be a compromise between the amount of metal active sites and the negative influence of larger particle size at higher loadings. Malik et al. [32] examined multi-walled carbon nanotubes (MWCNTs) as support for Cu₂O. The highest current density in the potential range of -0.2 to -1.8 V was obtained at 30% Cu₂O, where methanol was the major product. The superior activity of Cu₂O supported on MWCNTs was attributed to an increase in the active surface area and improved accessibility to the active sites for reactants. Furthermore, MWCNTs offered reaction sites for CO₂ and trapped electrons that increased the conversion rate of CO₂⁻ to desired products. An improvement in catalytic stability was also observed, which makes it a promising candidate for CO₂ reduction to methanol. Genovese et al. [12] investigated various electrocatalysts with transition metals supported on CNTs. It was found that Cu/CNT performed worse for C₁-C₃ production compared to CNT supported Pt and Fe, which is in contrast to the higher activity obtained for Cu foil. Baturina et al. [5] studied the activity of Cu nanoparticles supported on carbon black, single-walled carbon nanotubes (SWCNTs) and Ketjenblack (KB) for hydrocarbon production via CO₂RR. They found that carbon supported Cu nanoparticles were more selective towards C₂H₄ generation than electrodeposited smooth Cu film. Moreover, it was found that the carbon support could activate hydrogenation at potentials more negative than -1.2 V, which could promote CH₄ formation. The ratio of C₂H₄/CH₄ faradaic efficiency decreased with a decrease in Cu particle size. This was attributed to an increase in the number of low-coordinated sites. Therefore, based on the previous discussion, it can be concluded that CO₂RR over Cu-based catalysts is very complex. Several factors may determine the performance of the Cu-based materials, such as the physicochemical properties of the Cu-based material and support as well as experimental aspects.

2.3 Catalyst preparation by homogeneous deposition precipitation (HDP)

The active surface area per unit volume of catalyst defines the activity of solid catalysts and smaller particles can improve the activity per unit volume. However, such small particles of an active species alone do not provide thermostable and highly active catalysts, since they tend to sinter during treatment procedures that are usually conducted at relatively high temperatures [42]. Sintering is the process of agglomeration of sites resulting in the loss of reactive surface

area. Therefore, supports, highly porous and thermostable materials, are utilised in order to stabilise the active particles of solid catalysts and improve the thermal stability.

The procedures of the production of supported catalysts can be divided into two groups [13]: (1) simultaneous synthesis of the support and the active component(s) from a mixture of their precursors typically called co-precipitation; (2) and deposition of the precursor of the active component(s) onto a separately produced support. One of the most successful examples of the first procedure is the technical ammonia synthesis catalyst, which is produced from magnetite (Fe_3O_4) containing a small percentage of alumina. Reducing the alumina containing magnetite to remove the oxygen leads to a porous material, in which metallic iron particles are separated by the alumina particles. Although during co-precipitation the active component and the support are usually very well dispersed, it is difficult to control the porous structure and the mechanical strength of the resulting catalyst. A wide number of supports are commercially available that have diverse size, shape, structure, physicochemical properties, and mechanical properties.

Deposition-precipitation is a technique, developed by Geus et al. [13; 14] where the active precursor is loaded onto a support by precipitation. This results in a uniform distribution of the active precursor over the support and is an attractive option for the synthesis of catalysts. Sufficiently large interaction between the nuclei of an insoluble active precursor and the surface of a suspended support can bring about precipitation of the precursor at the surface of a support. Thus, the surface of a support functions as a seed for the nucleation and the introduction of a support into a solution causes either a reduction of surface free energy of tiny nuclei or stabilisation of the precipitate, decreasing the energy barrier for nucleation.

Nucleation of the metal species is generally induced by changing the pH of a solution so compounds with a low solubility are formed. When this is done by injection of the precipitant, great care must be taken to prevent local concentrations exceeding the critical supersaturation [13], which would cause bulk precipitation. Therefore, homogeneous deposition precipitation (HDP) methods are often preferred, whereby precipitation is induced homogeneously throughout the reaction vessel.

Precipitation by raising the pH level can be used with the preparation of many catalysts. Typically, the support is suspended in a solution of the metal nitrate and a compound is added that can consume hydrogen ions. Urea can be utilized to increase the pH of the suspension. Urea reacts according to the following reactions [13]:



The reaction in which urea first reacts to produce cyanate and subsequently to ammonium, carbon dioxide, and hydroxyl ions, exhibits at temperatures above about 330 K (57 °C). Mixing can therefore be carried out at room temperature, while the generation of hydroxyl ions proceeds at higher temperatures. The use of urea, however, does not necessarily lead to the uniform loading of the support. The interaction of a precursor and a support is essential to the method of deposition precipitation [13]. When the interaction is too strong, mixed metal – support phases are formed, whereas a too weak interaction, results in large, unsupported particles.

3 Experimental

3.1 Materials and equipment

All the materials and chemicals were used as received from the suppliers without any further purification treatments, unless specifically mentioned. Deionised water ($>18 \text{ M}\Omega \text{ cm}$ resistivity), made by Millipak® Express 40 Milli-Q unit, was used throughout the work. The details concerning chemicals and gases used during experimental procedures are summarised in table 3.1. Standard glassware and other laboratory materials were employed for much of the work with the specialised equipment detailed in table 3.2.

Table 3-1. Summary of chemicals used for catalyst synthesis and catalytic testing.

Chemical name	Chemical formula	Purity and Supplier
Carbon Dioxide gas	CO_2	99.999%, Tianjin Co., Ltd
Carbon paper	CP	TGP-H-060, Toray Corporation
Copper (II) nitrate trihydrate	$\text{Cu}(\text{NO}_3)_2 \cdot 3\text{H}_2\text{O}$	$\geq 99\%$, Acros Organics
Deuterium Oxide	D_2O	99.9%, Beijing Inoke technology Co., Ltd
Dimethyl sulfoxide	$(\text{CH}_3)_2\text{SO}$	Beijing Inoke technology Co., Ltd
Gas mix	10% H_2 , 90% Ar	Tianjin Co., Ltd
Ketjenblack EC-600 JD	KB	$>99.9\%$, AkzoNobel
Methyl Alcohol	CH_3OH	$\geq 99.5\%$, General-Reagent
Multiwall Carbon nanotubes long 1020	MWCNT1020	$>97\%$, Shenzhen Nanotech Port
Multiwall Carbon nanotubes long 2040	MWCNT2040	$>97\%$, Shenzhen Nanotech Port
Nafion membrane	Nafion117	DuPont
Nafion solution	$\text{C}_7\text{HF}_{13}\text{O}_5\text{S} \cdot \text{C}_2\text{F}_4$	5 wt.%, DuPont
Nitric acid	HNO_3	$\geq 65\%$, AnalaR NORMAPUR
Nitrogen gas	N_2	99.999%, Yara Praxair
Potassium hydrogen carbonate	KHCO_3	99.7-100.5%, Alfa Aesar
Standard gas mix	$\text{CO}_2, \text{CH}_4, \text{C}_2\text{H}_4, \text{C}_2\text{H}_6, \text{H}_2, \text{CO}$	Tianjin Co., Ltd
Urea	$\text{CH}_4\text{N}_2\text{O}$	99%, VWR International

Table 3-2. Summary of equipment used for catalyst synthesis and catalytic testing.

Instrument name	Model	Manufacturer
Analytical balance	MS104S, ME204	Mettler Toledo
CNC stirrer	MS-H-PRO+	Longxin Smart Equipment Co., Ltd
Electrochemical workstation	CHI 760D	Shanghai equipment Co., Ltd
Furnace	BTF-1200C	BEQ Equipment, Ltd
Gas flowmeter	CS200-A	Beijing create electronic, Ltd
GC	GC 9790II	Zhejiang analysis instruments, Ltd
NMR	ASCEND 400M	Bruker Corporation
pH meter	SEVEN COMPACT S220	Mettler Toledo
Raman	HORIBA EVOLUTION	Horiba Jobin Yvon S.A.S.
SEM	VERIOS 460L	US FEI Co.
Stirring hot plate	SUPER-NUOVA™	Thermo Scientific
Stirring hot plate	IKA RCT	IKA Laboratory Equipment
TGA	STA6000	Perkin Elmer, Inc.
Ultrasound cleaner	USC-TH	VWR International
Ultrasound cleaner	KQ-100	Kunshan ultrasound instruments Co., Ltd
XPS	ESCALAB™ 250XI+	Thermo Fisher Scientific
XRD	AXS D8 ADVANCE	Bruker Corporation

3.2 Electrode fabrication

3.2.1 Catalyst synthesis

Three different carbon materials were utilised as support, i.e. Ketjenblack and two types of MWCNTs of different outer diameter. Associated characteristics declared by retailers are represented in the table 3-3. Industrially manufactured carbon materials may contain traces or some levels impurities of metal oxides such as MnO₂ and CuO_x. Certain authors consider those impurities to be catalytically active towards reduction of carbon dioxide [31], acknowledging probable impact for catalytic performance due to reduction of metal oxides to metal forms during electrochemical processes.

Table 3-3. Main characteristics of MWCNTs and Ketjenblack supports [28; 43].

Support material	Main diameter range, nm	Length, µm	Primary particle radius, nm	BET specific surface area, m²g⁻¹
MWCNT1020	10 – 20	> 5		100 – 160
MWCNT2040	20 – 40	> 5		80 – 140
Ketjenblack EC600JD			34.0	1270

In this work, beforehand the deposition procedures, MWCNT supports were refluxed in concentrated nitric acid for three hours at 90 °C in order to remove all possible impurities and provide with functional groups. Hereafter, the materials were washed with necessary amounts of DI water until the neutral pH value of water passing through the materials was achieved. Drying was performed at 90 °C overnight. The pre-treatment could not be done for the Ketjenblack support due to swelling of the material upon emersion in acid. This could be related to the very high surface area.

In a typical catalyst synthesis procedure, a calculated amount of copper nitrate trihydrate, urea and nitric acid were dissolved in the determined volume of deionized water to obtain an aqueous precursor solution with a specific blue-green colour. Carbon supports were suspended into the desired volume of the precursor solution in a three neck round bottom flask and the colloid solution was heated from room temperature up to 90 °C and maintained for 18 hours for the metal precipitation to take place under continuous stirring and corked reflux condenser. An image of the experimental setup used for catalyst preparation is shown in Figure A1, Appendix 1.

The pH of the suspension increased from the initial value of 2 to approximately neutral value after the deposition time. Furthermore, the solution colour changed to transparent, indicating the successful precipitation of the precursor metal. Subsequently, the suspension was cooled down to the room temperature, thoroughly washed with the deionized water and placed in the oven for drying at 90 °C overnight (12 hours).

Different amounts of copper nitrate trihydrate, correlated by molar weight ratio to the mass of support material, was used to achieve different copper loading. The prepared samples were denoted according to the associated type of support material and metal loading as summarized in Table 3.4.

Table 3-4. Denotations of the synthesised catalysts.

Catalyst denotation	Cu loading (wt. %)	Support material
5Cu/MWCNT2040	5	MWCNT2040
10Cu/MWCNT2040	10	MWCNT2040
20Cu/MWCNT2040	20	MWCNT2040
20Cu/MWCNT1020	20	MWCNT1020
20Cu/KB	20	Ketjenblack EC600JD

When the catalytically active component is desired to be in the metallic state, reduction shall be carried out after the calcination step. Both calcination and reduction are thermal treatment processes applied to solid materials in order to bring about a composition change. Looking ahead this work, $(CuOH)_2CO_3 + N_2 \xrightarrow{^\circ C} 2CuO + CO_2 \uparrow + H_2O$ happens during “calcination” stage and $CuO + H_2 \xrightarrow{^\circ C} Cu + H_2O$ during “reduction” phase.

All the as-prepared samples were exposed to thermal treatment procedures employing a quartz reactor with a gas supply and a tubular furnace. First, samples were exposed to nitrogen atmosphere for 3 hours at 400 °C, with a 5 degrees per minute temperature increase from room temperature. Subsequently, a reduction of the materials was accomplished in a flow of 10% hydrogen and 90% argon gas mixture also at 400 °C for 3 hours and 5 degrees per minute temperature increase. In this work, only the reduced catalysts were utilized for electrochemical reduction experiments.

3.2.2 Catalyst ink preparation

Catalyst coated Toray carbon paper (CP) was used as electrode during cyclic voltammetry and chronoamperometry investigations. It is a Teflon treated fiber composite, possessing hydrophobic properties and thus suitable as an electrode support material. Toray carbon paper of TGP-H-060 type was utilised as a backing material for its surface modification with catalyst ink. Prior to modification, the carbon paper was clipped to uniform 1.5 cm² fragments, stored in purified deionised water.

After a set of investigational tests, an optimal combination of experimental procedures for catalyst ink preparation was established. Two milligrams (2 mg) of catalyst powder was dispersed in 40 µL of deionised water and 60 µL of 5 wt.% Nafion ethanol-based solution inside a centrifuge tube and exposed for 40 min in ultrasonic bath. Later, 1 cm² area of both sides of carbon paper was coated, in sequence assisted by a micropipette, with 50 µL of catalyst ink and suspended for drying in air for at least 1 hour. Hereafter, the material was exposed to 0.5 molar KHCO₃ solution for a short time to confirm chemical stability of catalyst surface.

3.3 Catalyst characterization procedures

Thermal gravimetric analysis (TGA) is a method of thermal analysis for material characterization in which the mass of a sample is measured during a temperature change in an atmosphere of desired gas flowing in a system. TGA was conducted using the Perkin Elmer

STA 6000 apparatus at a heating rate of 10 °C min⁻¹ from room temperature to 830 °C under flowing air atmosphere.

The morphology of materials was characterized by scanning electron microscopy (SEM). The SEM images were obtained on a FEI Verios 460L operated at an acceleration voltage of 20 kV.

Powder X-ray diffraction (XRD) study of the catalysts was performed by Bruker-AXS Micro-diffractometer (D8 ADVANCE) using a Cu K α radiation source ($\lambda = 1.5406 \text{ \AA}$, 40 kV and 40 mA). The XRD patterns were recorded with 2 Theta range from 5 degrees to 90 degrees with a step interval of 2 °/min. The characteristic peaks were indexed according to the Joint Committee on Powder Diffraction Standards (JCPDS) database. The crystallite size was estimated by the Scherrer equation (Eq. 3.1).

$$d_c = \frac{K \times \lambda}{\beta \times \cos \theta} \quad (3.1)$$

Where d_c is average crystalline size, K is a dimensionless shape factor depending on the actual shape of the crystallite, λ is the X-ray wavelength, β is line width at the half of a maximum intensity, and θ is the angle of incidence (Bragg angle).

The Raman spectra were obtained with the use of Horiba Evolution, Czerny Turner total reflection spectrometer equipped with a three-dimensional confocal microscope with a focal length of 800 mm and applying aberration correction.

X-ray photoelectron spectroscopy (XPS) analysis was performed using ESCALAB 250XI system applying a monochromatic Al K α acquisition X-ray source. High resolution spectra were obtained via pass energy of 30.0 eV and an energy step size of 0.1 eV. Atomic percentage (at%) of each constituent element of materials' composition was used in order to define weight percent (wt. %) of corresponding chemical element with the use of the following formula (Eq. 3.2):

$$\text{wt}\% = \frac{\text{at}\%_i \times A_{r_i}}{\sum P_i} \times 100\% = \frac{P_i}{\sum P_i} \times 100\% \quad (3.2)$$

Where A_{r_i} is the atomic weight of a chemical element, i.e.: Carbon, Oxygen and Copper, and its multiplication with a corresponding value of the atomic percentage results in, so called, P-value.

3.4 Activity tests

3.4.1 Cyclic voltammetry

Cyclic voltammetry (CV) has become a popular technique for initial electrochemical studies of new systems [22]. During a typical experiment, the working electrode potential is swept in both positive and negative directions. The electric current is recorded as a function of applied potential to generate cyclic voltammogram, which shows current amplification and peaks when electrochemical oxidation and reduction occurs. Prior to the experiments, the cells were purged with CO₂ or N₂ gases for at least 30 min, allowing adequate dissolution to occur. An image of three-electrode experimental setup is represented on a figure A2 Appendix A. In a typical CV sweep, a scan rate of 50 mV was selected for a potential range from 0.2 V to -1.4 V.

3.4.2 Chronoamperometry

Unlike cyclic voltammetry, this research method involves the application of fixed potential at the electrodes. The resulting electric current recorded as function of time to produce chronoamperograms. Potentiostatic measurements were performed in a H-type electrochemical cell represented on a figure A3. Two compartments were separated by a proton conducting Nafion117 membrane, modified carbon cloth acted as a working electrode and the Ag/AgCl reference electrode was utilised. Submerged for approximately 1 cm² platinum (Pt) plate represented counter electrode. A 30 mL volume of each compartment was employed to occupy with a 0.5 molar aqueous solution of potassium hydrogen carbonate and carbon dioxide gas was continuously supplied to the system during electrolysis at 5 mL.min⁻¹ flow rates. After 30 min initial saturation, pH of the electrolyte reached 7.2 and this value was used for correlation of voltage to reversible hydrogen electrode. All the electrochemical experiments were performed at room temperature and atmospheric pressure. The potentials in this work, unless mentioned, are reported with respect to RHE calculated based on (Eq. 2.1).

3.5 Analytical chemistry techniques

CO₂RR can generate a range of products in both liquid and gas phase. The most common gas phase products of CO₂RR are hydrogen from competing hydrogen evolution reaction (HER), carbon monoxide (CO), and hydrocarbons (CH₄, C₂H₄). Possible liquid phase products typically include different oxygenates such as alcohols, formate, and formic acid. Consequently, the diversity of products that might be produced simultaneously requires the use of multiple product quantification methods.

3.5.1 Gas Chromatography

To analyse the gas phase products, the gas outlet of the cathodic compartment was connected to the gas chromatograph (GC) for periodical sampling. The gas products were quantified by a Puretek instruments GC9790II. Gas aliquots were collected from the headspace of the cathodic compartment with a cycle interval of 20 minutes and injected into a gas chromatograph. Volatilization of a gas sample happens in an injector, followed by the separation of mixture's components in a specially prepared column, where the sample is carried by the carrier gas. Subsequently, the identification of each gas component is carried out by either a thermal conductivity detector (TCD) or flame ionization detector (FID). The gases were analysed by the two types of detectors are as follows:

1. Hydrogen and carbon monoxide gases were detected by a TCD, that measures changes in thermal conductivity of the gas phase
2. FID was utilized to detect traces of hydrocarbons gases, i.e. CH₄, C₂H₄ and C₂H₆.

The GC instrument was calibrated using standard gas mixture with the following composition: CH₄ – 0.51%, C₂H₄ – 0.49%, C₂H₆ – 0.53%, H₂ – 1%, CO – 1,07% and remaining CO₂ (93.4%) for product quantification by standard normalisation method. The Faradaic efficiencies of the gaseous products were calculated using the equations:

$$FE = \frac{n_i \times F \times Y_i \times F_m}{I} \quad (3.3)$$

$$F_m = \frac{P \times F_v}{RT} \quad (3.3)$$

where molar flow rate F_m is defined by the pressure P , the volumetric flow F_v , the universal gas constant R and temperature T . Faradaic efficiency (FE) of a product is defined by the electron transfer coefficient of the product n_i , the Faraday's constant F , the fraction of the product Y_i , the molar flow F_m , and the average magnitude of current I at a sampling time.

3.5.2 Nuclear Magnetic Resonance (NMR)

The liquid phase products were analysed by Nuclear Magnetic Resonance (Ascend 400M, Bruker) spectroscopy, by withdrawing 10 mL of the electrolyte solution after CA measurements. This is a useful technique for detection of electrochemical products since it could be performed directly on the electrolyte solution without a need for removing the electrolyte ions. The operating principle [3] is based on absorbing and reemitting of electromagnetic radiation by a nuclei in a magnetic field. NMR spectroscopy provides the identification of the protons

appearing in different chemical species, present in an experiment sample. The resulting characteristic peaks are unique for each compound and their magnitude, related to an internal standard, can be utilized to determine their concentrations.

Dimethyl sulfoxide (DMSO) was employed as an internal standard for products identification and quantification. Typical experimental procedure was conducted as follows: 0.8 mL of the electrolyte containing CO₂ reduction products after several hours long electrolysis, 0.2 mL of DMSO and 0.2 mL of deuterium oxide (D₂O) were transferred into a centrifuge tube, well intermixed and thereafter half of the mixture, i.e. 0.6 mL, was separated into a NMR sample tube. During the spectroscopy experiment, solvent suppression was utilized to decrease the intensity of the water peak.

4 Results and discussion

4.1 Catalyst characterization

4.1.1 Thermal gravimetric analysis

Figure 4.1 displays the thermogravimetric analysis curves of calcined materials in a flow of air, and Table 4.1 summarizes the weight loss detected during TGA experiment. TGA analysis confirms the graphitic order of the materials, as well as their high purity, since all the materials lost their weight over a narrow temperature range [16]. The decomposition of materials started at the temperatures above 400 °C. Therefore, 400 °C was chosen for calcination and reduction of the catalysts. It can be seen from Table 4.1. that the materials containing 10 wt.% and 5 wt.% Cu exhibited greater weight loss during TGA than the materials with 20 wt.% Cu loading. This is expected as there will be a higher amount of Cu residue after TGA experiment.

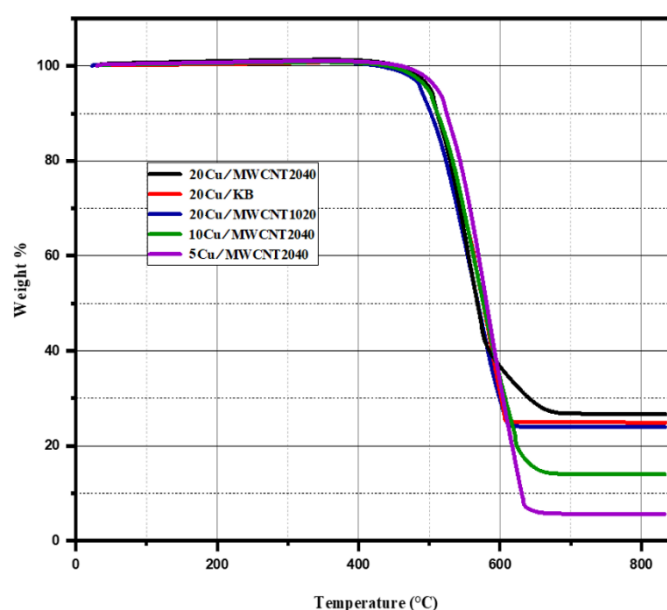


Figure 4.1. TGA curves of calcined materials in a flow of air.

Table 4-1. TGA curves in a flow of air of calcined samples.

Catalyst	Weight loss (%)	d_{Cu} (nm) ^a
20Cu/KB	75.12	30
20Cu/CNT1020	76.03	27
20Cu/CNT2040	73.34	28
10Cu/CNT2040	85.99	22
5Cu/CNT2040	94.36	14

^a Calculated from the Cu(111) peak.

4.1.2 SEM analysis

The SEM images of the calcined and reduced 20Cu/MWCNT1020 catalyst is presented in Figure 4.2 (a) and (b), respectively. It is evident that the Cu particles are coated on the surface of the MWCNTs. Furthermore, the Cu particles are highly dispersed on the MWCNT support after calcination. Hossain et al. [20] also found that the HDP method resulted homogeneous coating of Cu on the surface of MWCNT. Agglomerations of copper particles of micrometre dimensions could be also seen from Figure 4.2. Compared to the calcined catalyst, a decrease in porosity is also seen after reduction.

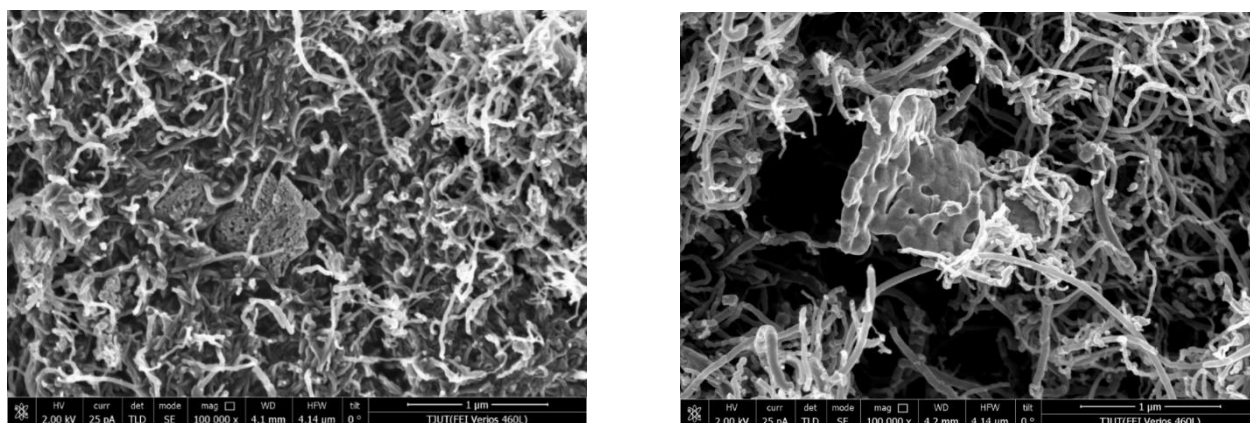


Figure 4.2. SEM images of the calcined (a) and reduced (b) 20Cu/MWCNT1020 catalyst.

4.1.3 X-ray diffraction

The carbon supported Cu catalysts was investigated by XRD after preparation by HDP, after calcination, and after reduction, and the corresponding XRD patterns are presented in Figure 4,3 (a)-(c). The diffraction present at 2 thetas of 26.2°, 42.2°, and 44.4° for the MWCNT supported catalysts are attributed to carbon (PDF 75-1621). No clear peaks are observed for carbon for the 20Cu/KB catalyst, because of the amorphous nature of the KB material. For all catalyst, peaks corresponding to $\text{Cu}_2(\text{OH})_2\text{CO}_3$ (PDF 41-1390) is present after HDP procedures. These peaks increase in intensity for the MWCNT2040 supported catalysts for higher Cu loading as expected. The peaks are much less intense for the 20Cu/MWCNT1020 catalyst, which indicates higher dispersion or lower degree of crystallization. Similarly, the peaks of CuO is also present for all catalysts (PDF 44-0706). It can also be seen that the peak intensity of CuO and $\text{Cu}_2(\text{OH})_2\text{CO}_3$ are connected. The CuO phase could have been formed by the oxolation reaction in which Cu hydroxide species are transformed into CuO [9].

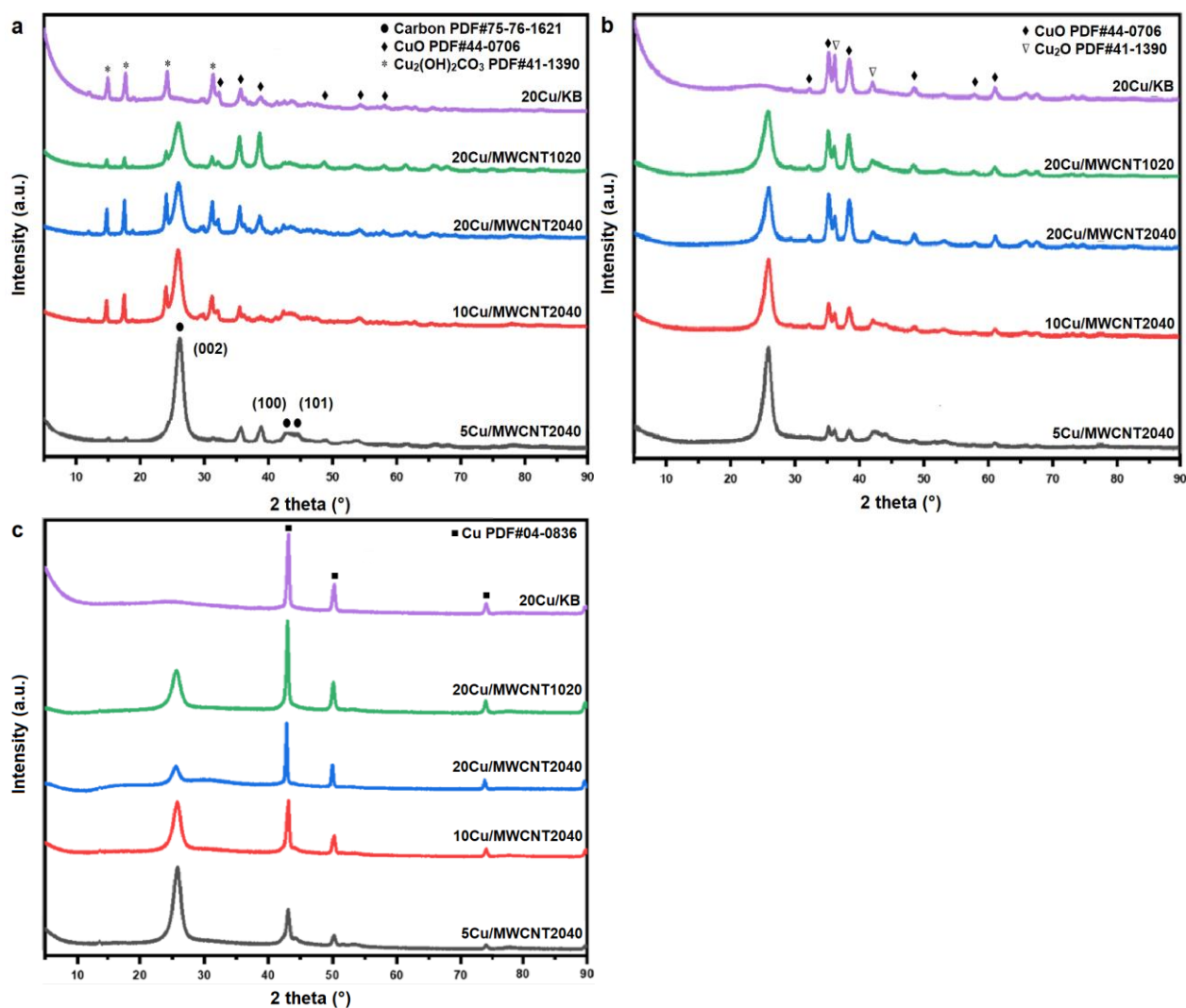


Figure 4.3. XRD patterns of Cu supported on different carbon materials after HDP (a), calcined (b) and reduced (c).

The peaks of CuO are still present after calcination for all catalysts (Figure 4.3. b). A slight increase in peak intensity is observed compared to the spectra after HDP. In addition, peaks corresponding to Cu₂O (PDF 05-0667) are also observed. This means that there is a mixture of CuO and Cu₂O phases present after calcination. As can be seen from Figure 4 (c), the Cu oxide phases are completely reduced after reduction to metallic Cu (PDF 04-0836). Interestingly, the peak intensity of 20Cu/MWCNT2040 is lower compared to that of 20Cu/KB and 20Cu/MWCNT1020 despite having higher intensity of CuO before reduction. The Cu crystallite size calculated by the Scherrer equation (Eq. 3.1) of the reduced catalysts are summarized in Table 4-1. As can be expected, the crystallite size increase with higher Cu loading. The 5Cu/MWCNT2040 had the smallest crystallite size of 14 nm, while the crystallite size of samples containing 20 wt. % Cu were comparable around 26–30 nm.

4.1.4 Raman spectroscopy

Raman spectroscopy is a popular, non-destructive chemical analysis technique which provides information about chemical structure, phase, crystallinity and molecular interactions. The Raman effect results from the interaction of laser light with molecular vibrations within the sample and it can be used for structural characterization of any carbon systems. Figure 4.4 shows the Raman spectra for the 20/MWCNT2040 catalyst after calcination and reduction.

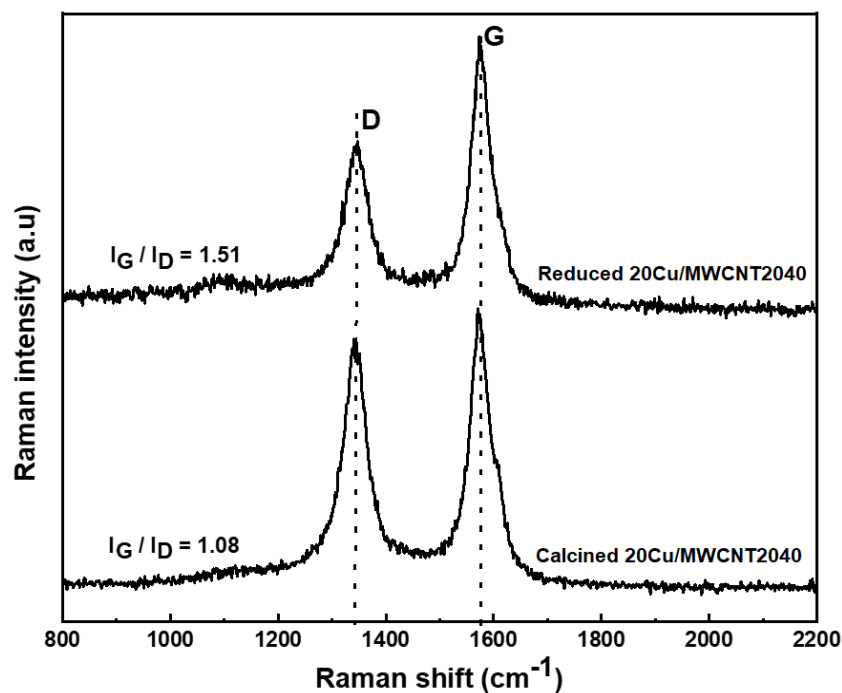


Figure 4.4. Raman spectra over calcined and reduced 20% Cu/MWCNT2040.

Carbon materials show two common features in their Raman spectra in the region from 800 to 2000 cm⁻¹, namely the G and D peaks, which lie at ca. 1560 and 1360 cm⁻¹, respectively [11]. In addition, D-band and G-band have been attributed to disorder-induced and graphitic features, respectively [50]. In other words, D-band represents disorder vibrations on the graphite wall of the carbon nanotubes, while the G-band are related to asymmetrical surface vibrations on graphite that originates from the ordered structure. Hence, the ratio of the magnitude of intensity of G-band to that of the D-band (I_D/I_G) corresponds to the defect density of the carbon material [8]. Compared to $I_D/I_G = 1.08$ for the calcined sample, the reduced sample shows much increased ratio of intensities, equal to 1.51. Therefore, this signifies a higher degree of crystallinity and structural order for the reduced sample.

4.1.5 X-ray photoelectron spectroscopy

XPS analysis of the catalyst was performed after ex situ pre-treatments as described in section 3.2.1. Figure 4.5 shows the Cu_{2p} spectra (a), C1s region (b), O1s region (c), and the XPS survey (d) of calcined and reduced 20Cu/MWCNT2040 and reduced 20Cu/MWCNT1020. The peaks used for fitting the Cu_{2p} spectrums was taken from Beisinger et al. [6]. The binding energy of Cu and Cu₂O is very close (932.61 eV vs. 932.43 eV), which makes it difficult to distinguish these species. However, the peak at approximately 932.5 eV is assigned to Cu₂O since a Cu₂O phase is detected by XRD. Peaks corresponding to Cu⁰ and Cu²⁺ can be identified after reduction. There could also be Cu⁺ species present after reduction. It can be observed that the Cu²⁺ fraction is higher for 20Cu/MWCNT1020 compared to 20Cu/MWCNT2040.

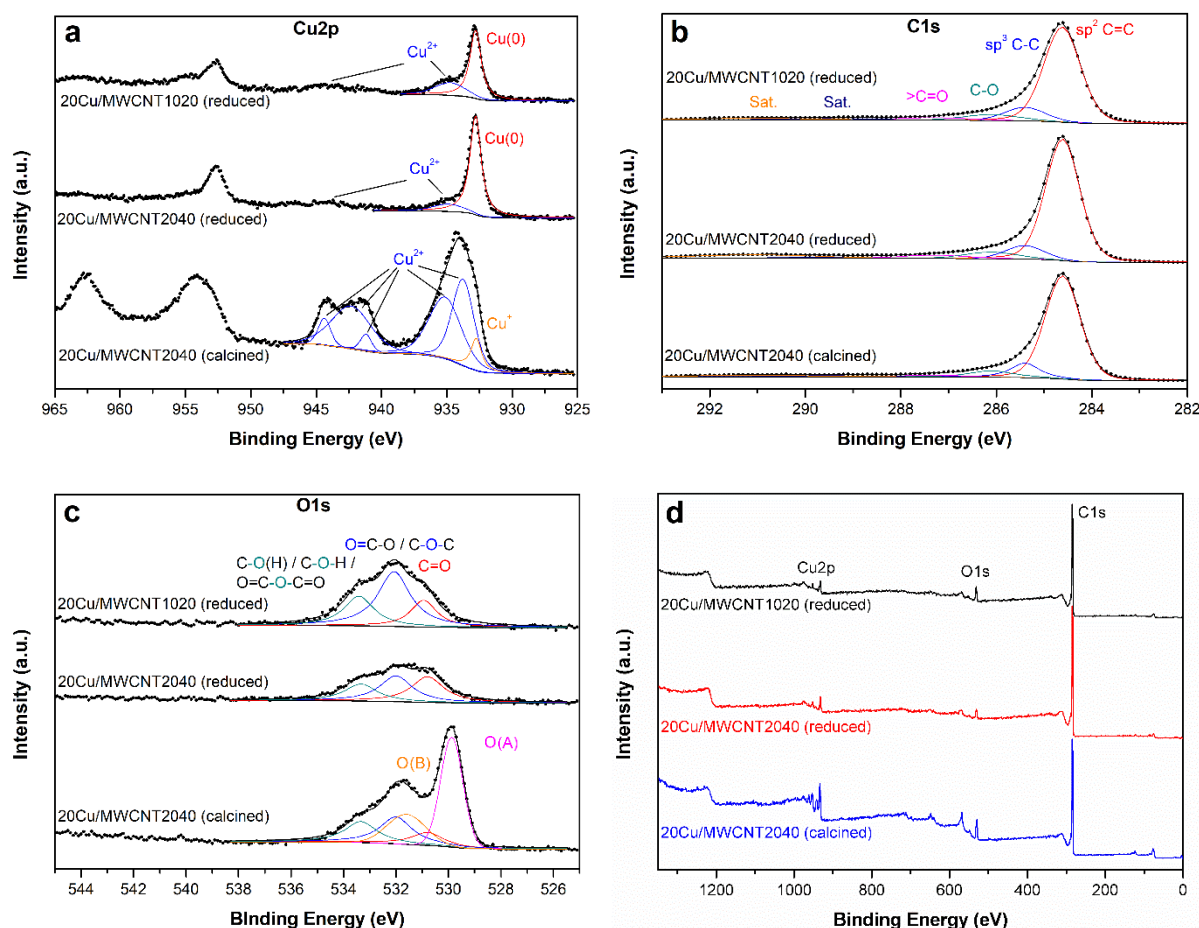


Figure 4.5 XPS spectra of reduced and calcined 20Cu/MWCNT2040 and reduced 20Cu/MWCNT1020 (a) Cu_{2p}), (b) C1s, (c) O1s, and (d) survey spectra.

The C1s region of the catalyst was fitted according to fitting parameters given by Zielke et al. [52]. It can be seen from Figure 4 (b) that the C1s spectra of the investigated samples are very similar. Table 4.2 summarizes the results of the XPS analysis, and it is found that the

distribution of carbon species is comparable for these samples. As expected, the O1s spectra of the calcined 20Cu/MWCNT2040 catalyst contain both oxygen species related to Cu oxides and the MWCNT support. The O (A) peaks corresponds to lattice oxygen species and the O (B) to hydroxide, hydrated, or defective oxygen sites of CuO and Cu₂O [6]. It can be seen that the distribution of oxygen species for the reduced catalysts are different, where the 20Cu/MWCNT1020 have a higher quantity of O=C-O or C-O-C species. From the survey spectra in Figure 4 (d) only carbon, oxygen, and Cu could be detected.

The surface composition was calculated by Eq. 3.2. and the results are also included in Table 4.2. The weight percentage of Cu for the calcined 20Cu/MWCNT support is in the close vicinity to the desired magnitude of 20%. After reduction, a lower Cu surface concentration is measured and the reason for this is not known. Deposition on KB support results in lower surface concentration than for Cu supported on MWCNTs.

Table 4-2. Summary of surface composition and distribution of carbon and oxygen species.

Catalyst	C1s (Binding energy, eV)				O1s (Binding energy, eV)			Composition (wt. %)		
	C=C 284.6	C-C 285.4	C-O 286.1	>C=O 287.3	(1) ^a 530.8	(2) ^a 532.0	(3) ^a 533.3	C	O	Cu
20Cu/MWCNT1020 ^b	77 %	12 %	7 %	4 %	21 %	53 %	26 %	85.1	7.6	7.3
20Cu/MWCNT2040 ^b	79 %	10 %	7 %	5 %	37 %	38%	25%	89.8	4.7	5.5
20Cu/MWCNT2040 ^c	78 %	12 %	8 %	3 %	21 %	44 %	34 %	71.5	9.2	19.3
20Cu/KB ^b								92.3	5.8	1.9

^a (1) C=O, (2) C-O-C or O=C-O, and (3) C-O (H) / C-O-H or O=C-O-C=O ^b calcined catalysts; ^c reduced catalyst.

4.2 Evaluation of catalysts for ECR of CO₂

4.2.1 Cyclic voltammetry

To evaluate the performance of the carbon paper, the CV and current profiles were measured over the carbon paper without catalyst in CO₂ saturated electrolyte. Figure 4.9 (a) shows the CV profiles of the carbon paper and (b) the current density profiles at a fixed -0.88 V over 4500 s. The results of 20Cu/MWCNT1020 is included in the figures for comparison. The blank carbon paper shows a higher current density in CV measurements than the carbon paper modified by Cu supported on different carbon materials (Figure 4.7).

In contrast, when a fixed -0.88 V overpotential is applied, the current density is relatively constant at about 3 mA/cm² for the carbon paper. The cathodic current over the 20Cu/MWCNT1020 sample decreases rapidly until it levels off at ca. 800 s, reaching a current density of approximately 5 mA/cm² after 4500 s.

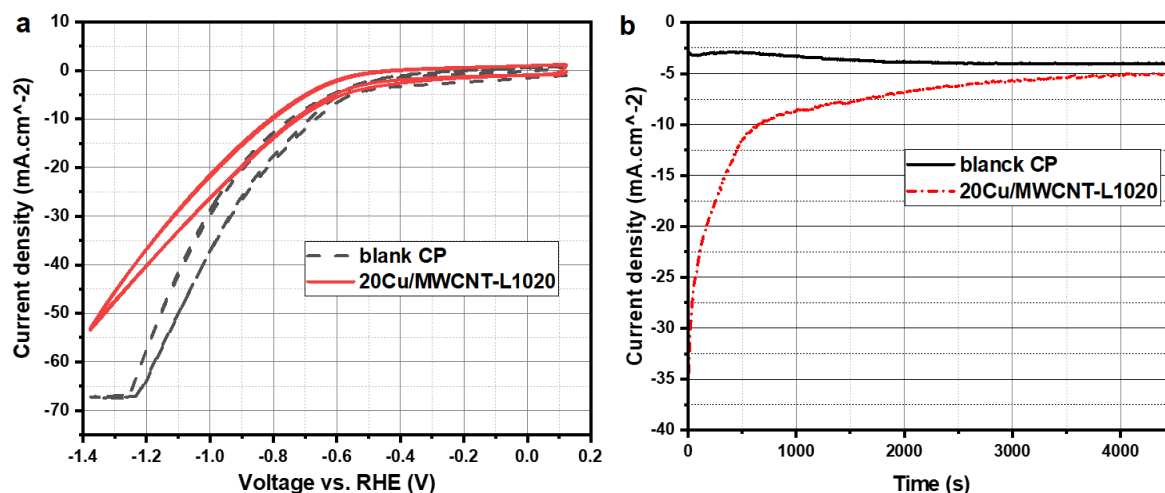


Figure 4.6. (a) CV profiles for blank CP versus modified CP with 20Cu/MWCNT2040 as WE in CO₂ saturated electrolyte and (b) current profiles obtained at a fixed potential of -0.88 V for 4500 s.

Figure 4.6 (a)-(e) shows the voltammetric curves for the carbon supported Cu catalysts (2mg, 1mg/cm²) in 0.5M KHCO₃ in N₂ and CO₂ atmosphere. The purpose of the measurements under N₂ saturation was to determine the influence of HER due to water electrolysis under the imposed negative overpotentials. The CV sweeps were performed by adjusting the voltage from 0.1 V and reducing it to -1.4 V before returning to 0.1 V. It can be seen that the current response for all catalysts are linear during CV in N₂ and CO₂ atmosphere. This suggests that the Cu phase remains stable in the investigated range. Furthermore, precipitation was not observed and the electrolyte remained clear during the experiments. These results suggest that the catalysts and electrolyte are electrochemically stable between 0.1 and -1.4 V in KHCO₃ electrolyte. The current density of the catalysts under N₂ atmosphere follows the order: 20Cu/KB > 20Cu/MWCNT2040 > 10Cu/MWCNT2040 > 20Cu/MWCNT1020 > 5Cu/MWCNT2040. A higher current density under CO₂ atmospheres is seen for all catalysts, which indicates that CO₂ reduction also takes place. In addition, the 20Cu/KB shows the highest current density of 72 mA/cm² in CO₂ saturated electrolyte, while the other catalysts have comparable current density around 55 mA/cm². The onset potential for HER and CO₂RR

is relatively similar for all catalysts (ca. -0.6 V) except for the 5Cu/MWCNT2040, which has an onset potential for the reactions around -0.7 to -0.8 V.

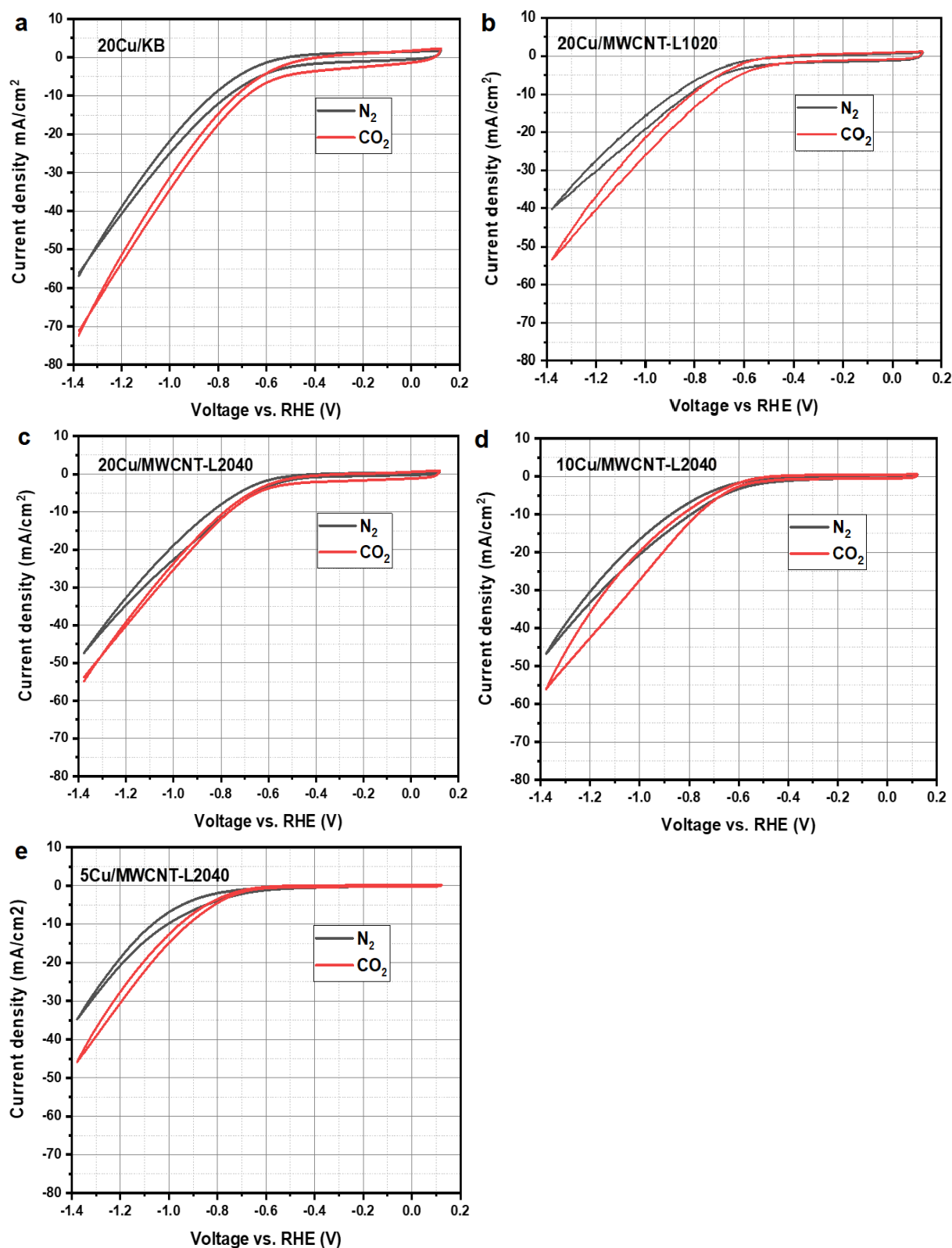


Figure 4.7. Cyclic voltammety profiles for 1 cm^2 catalysed carbon cloth with 2 mg of (a) 20Cu/KB, (b) 20Cu/MWCNT1020, (c) 20Cu/MWCNT2040, (d) 10Cu/MWCNT2040, and (e) 5Cu/MWCNT2040 0.5M KHCO_3 electrolytes purged with N_2 and CO_2 gases.

4.2.2 Chronoamperometry

Chronoamperometry was used to quantify the reaction products on the carbon-supported Cu catalysts, current versus time curves were recorded at -0.88 V. Figure 4.7 shows the chronoamperometry curves obtained over the catalysts. The cathodic currents decrease rapidly over the catalyst containing 10 and 20 wt% Cu, whereas it levels off more gradually for the 5Cu/MWCNT2040 sample. The current reaches the plateau faster for the 20Cu/MWCNT2040 catalyst at around 500 s compared to the other catalysts (around 1000 s). The cathodic current density of the catalysts does not agree with the CV curves in Figure 4.6. For example, the highest cathodic current density at constant potential is obtained over the 20Cu/MWCNT2040 catalyst, while the highest current density during CV was observed for the 20Cu/KB sample.

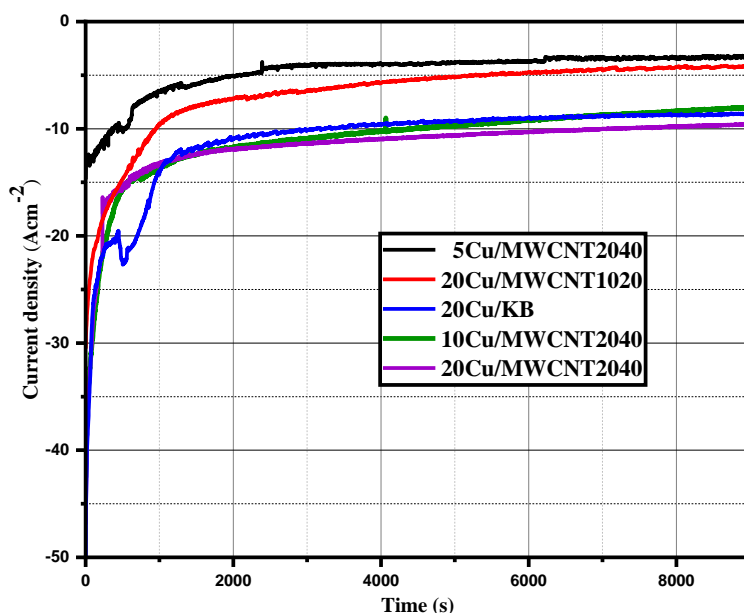


Figure 4.8. Chronoamperograms of 150 min electrolysis at -0.877 V vs. RHE using 5 different WEs in a CO_2 saturated 0.1 M KHCO_3 electrolyte with $5 \text{ mL}\cdot\text{min}^{-1}$ CO_2 flow.

The faradaic efficiency of the 5 catalyst was calculated to compare the catalysts at the same potential after 9000 s. The faradaic efficiency for the carbon-supported Cu catalysts is shown in Figure 4.8. As can be seen, the product with the highest faradaic efficiency is H_2 for all catalysts. In addition, HCOOH has the highest faradaic efficiency of the liquid products over the catalysts. The 20Cu/MWCNT1020 generates the highest amount of CH_3OH . This could be related to a higher oxygen content on the surface of the catalyst as shown by XPS. There are no clear trends in product generation for the MWCNT1020-supported catalyst with different Cu content. However, the total faradaic efficiency increases with Cu loading.

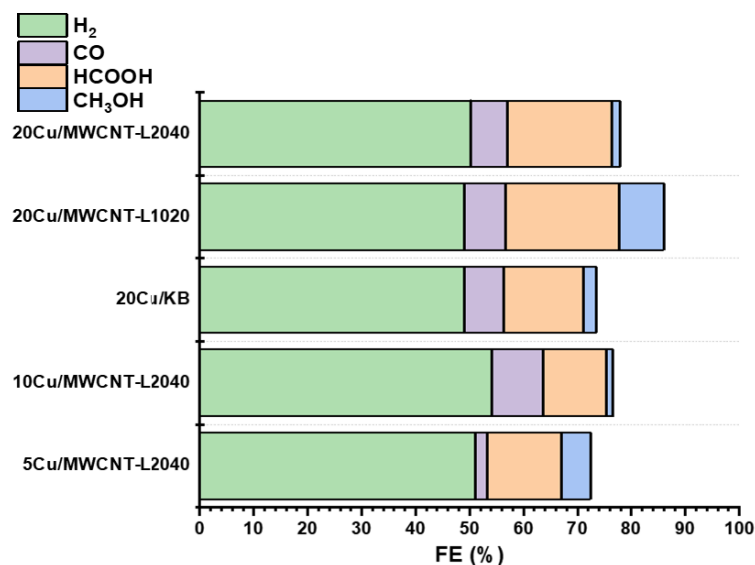


Figure 4.9. Faradaic efficiencies of identified products for carbon-supported Cu catalysts after 9000 s held at -0.88 V.

Current versus time curves were measured over the 20Cu/MWCNT1020 catalyst at different constant potentials of -0.5 to -1.2 V over 9000 s, and the results are shown in Figure 4.10. As the potential increases from -0.5 to -1.2 V, the current versus time curves shift to more negative values.

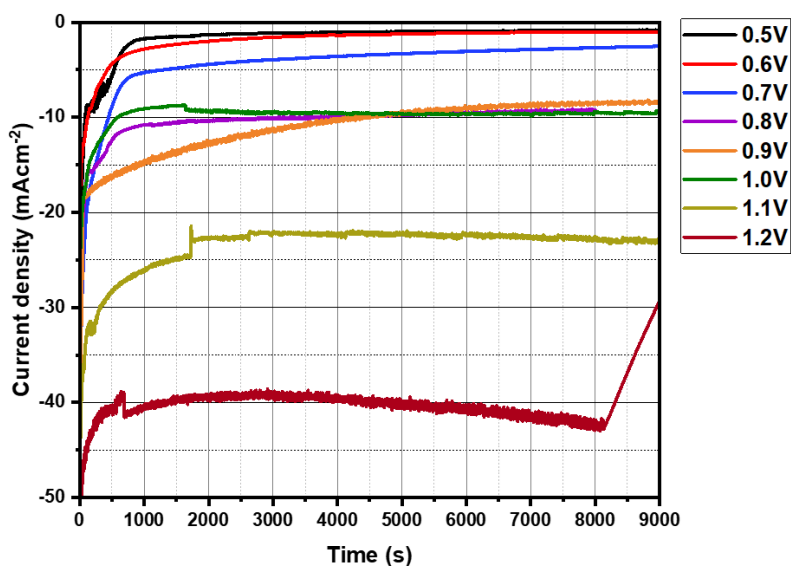


Figure 4.10. Chronoamperometric curves at potentials of -0.5 to -1.2 V vs RHE for 9000 s in CO_2 saturated KHCO_3 electrolyte over 20Cu/MWCNT1020.

The current density decreases until it reaches a plateau after an initial drop in the current density. It can be seen that the drop rate is much smaller at -0.9 V compared to the drop rate at other potentials. The change in current density in the initial phase can be attributed to changes

in chemical species on the electrode surface [5]. Hence, it appears that the stabilization time on the electrode surface is longer at -0.9 V.

Figure 4.11 shows the faradaic efficiency for H_2 , CO, HCOOH, and CH_3OH as well as the total faradaic efficiency versus potential for 20Cu/MWCNT1020. Significant differences in the CO_2 reduction product distribution is seen over the potential range of -0.5 to -1.2 V. The H_2 faradaic efficiency varies slightly from 50–56 %. The faradaic efficiency for CO decreases from 13 % to its minimum at -0.8 V and then remains relatively stable at 5 % thereafter. Generally, the faradaic efficiency of HCOOH increases until its maximum at -0.9 V and then varies around 15–20 %.

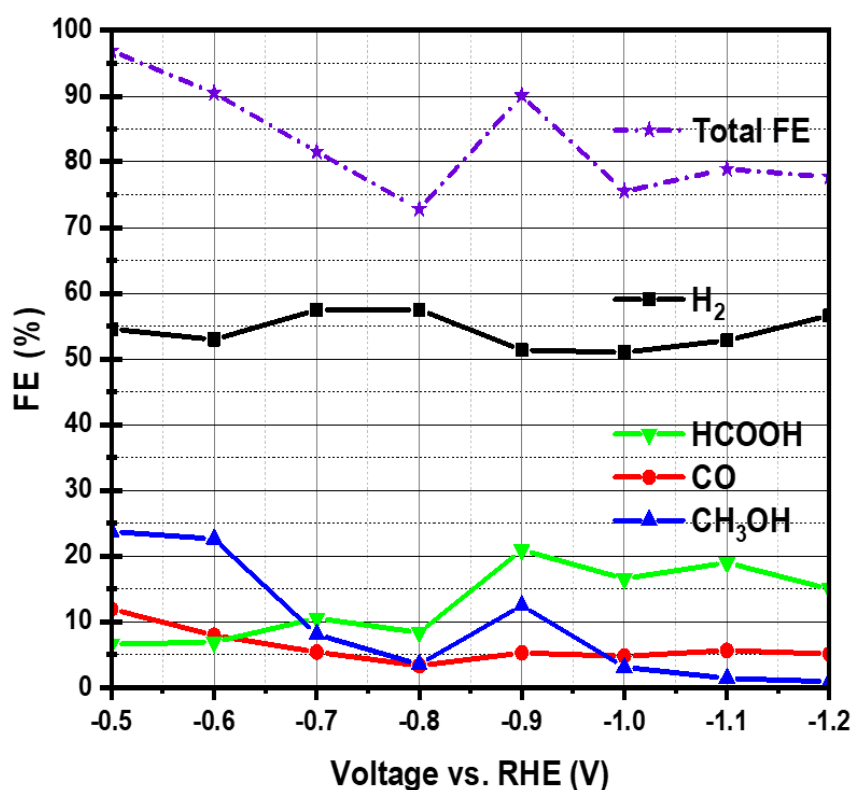


Figure 4.11. Faradaic efficiency for generation of H_2 , CO, HCOOH and CH_3OH over 20Cu/MWCNT1020 after 9000 s long electrolysis sets at different potentials.

In contrast, the faradaic efficiency of CH_3OH shows no clear trend. The faradaic efficiency of methanol is around 23% at low potentials before it decreases to 3 % at -0.8 V. Then it increases again to 13 % at -0.9 V before it levels off at higher potentials. The total faradaic efficiency also decreases initially before it reaches a new peak at -0.9 V at 90 % and then settles around 78 %.

5 Conclusions and future work

5.1 Conclusion

In this work, various Cu nanoparticles supported on MWCNT1020, MWCNT2040, and KB were synthesized using homogeneous deposition precipitation. The characterization indicated that this preparation method resulted in well-dispersed Cu nanoparticles after reduction. It was also found that the supports had different oxygen contents as well as oxygen species distribution. The activity of the catalysts was investigated for electrochemical reduction of CO₂ with emphasis on the formic acid (HCOOH) and methanol formation (CH₃OH). The highest faradaic efficiency for all catalysts was for H₂ generation, followed by HCOOH.

The effect of Cu loading was investigated over the MWCNT2040 (Cu = 5, 10, and 20 wt. %). It was found that the onset potential for hydrogen evolution and CO₂ reduction occurred at a higher potential at 5 wt. % Cu compared to 10 and 20 wt. % Cu. The total faradaic efficiency also increased slightly with increased Cu loading. The faradaic efficiency towards HCOOH was the highest at 20 wt. % Cu, while the 5 wt. % Cu sample achieved better efficiency for CH₃OH generation.

The total faradaic efficiency of different carbon supported 20 wt. % Cu followed the order MWCNT1020 > MWCNT2040 > KB. The faradaic efficiency for H₂ and CO generation was relatively similar for these catalysts and faradaic efficiency for HCOOH followed the same order as the total faradaic efficiency. However, the faradaic efficiency for methanol was significantly higher for the MWCNT1020 supported catalyst. A higher oxygen content was observed from XPS for Cu supported on MWCNT1020, which might play an important role in methanol production. Lastly, it can be concluded that the support had a higher impact on the catalytic performance than the Cu loading for the investigated catalysts.

5.2 Recommendations for future work

There is only a limited amount of studies that have investigated carbon supported Cu for electrochemical reduction of CO₂. In addition, several of the studies focus on the selective formation of hydrocarbons. Therefore, there is a significant amount of work that is needed before a suitable catalyst for selective production of HCOOH and CH₃OH can be realized. The use of a second metal or metal oxide could be attractive to discover more selective bimetallic or metal alloy catalysts.

Based on the literature review and the results from this work, there are several aspects that requires further study:

- 1) The hydrogen evolution reaction should be inhibited to enhance the faradaic efficiency towards the desired products.
- 2) The effect of Cu oxidation state should be investigated to determine its role in the formation of HCOOH and CH₃OH.
- 3) Further mechanistic insight on the pathways for HCOOH and CH₃OH production to determine how they are related and if the selectivity can be tuned towards one of the products.
- 4) Additional efforts needed to determine the effects of experimental conditions, i.e. electrolyte, electrolyte molarity, CO₂ source gas pre-wetting, system temperature, and catalyst loading on CP.

References

- [1] Administration, N. O. a. A. (2019). Global carbon dioxide growth in 2018 reached 4th highest on record. Retrieved from <https://www.noaa.gov/news/global-carbon-dioxide-growth-in-2018-reached-4th-highest-on-record>
- [2] Administration, U. S. E. I. (2019). Monthly Energy Review, May 2019. Retrieved from <https://www.eia.gov/totalenergy/data/monthly/pdf/mer.pdf>
- [3] Arnau Verdaguer Casadevall; Stephens, I. C., Ib. (2015). *Active Site Engineering in Electrocatalysis*. (Ph.D.), Technical University of Denmark (DTU),
- [4] Bard, A. J., & Faulkner, L. R. (2002). *Electrochemical Methods, Fundamentals and Applications* In: John Wiley & Sons, Inc, .
- [5] Baturina, O. A., Lu, Q., Padilla, M. A., Xin, L., Li, W., Serov, A., Artyushkova, K., Atanassov, P., Xu, F., & Epshteyn, A. J. A. C. (2014). CO₂ electroreduction to hydrocarbons on carbon-supported Cu nanoparticles. *4*(10), 3682-3695.
- [6] Biesinger, M. C., Lau, L. W., Gerson, A. R., & Smart, R. S. C. J. A. s. s. (2010). Resolving surface chemical states in XPS analysis of first row transition metals, oxides and hydroxides: Sc, Ti, V, Cu and Zn. *257*(3), 887-898. doi:<https://doi.org/10.1016/j.apsusc.2010.07.086>
- [7] Chang, T.-Y., Liang, R.-M., Wu, P.-W., Chen, J.-Y., & Hsieh, Y.-C. J. M. L. (2009). Electrochemical reduction of CO₂ by Cu₂O-catalyzed carbon clothes. *63*(12), 1001-1003.
- [8] Cooper, C., Young, R., & Halsall, M. (2001). Investigation into the deformation of carbon nanotubes and their composites through the use of Raman spectroscopy. *Composites Part A: Applied Science and Manufacturing*, *32*(3-4), 401-411.
- [9] Cudennec, Y., & Lecerf, A. J. S. s. s. (2003). The transformation of Cu(OH)₂ into CuO, revisited. *5*(11-12), 1471-1474. doi:10.1016/j.solidstatesciences.2003.09.009
- [10] Duan, X., Xu, J., Wei, Z., Ma, J., Guo, S., Wang, S., Liu, H., & Dou, S. (2017). Metal-Free Carbon Materials for CO₂ Electrochemical Reduction. *Advanced Materials*, *29*(41). doi:10.1002/adma.201701784
- [11] Ferrari, A. C., & Robertson, J. (2004). Raman spectroscopy of amorphous, nanostructured, diamond-like carbon, and nanodiamond. *Philosophical Transactions of the Royal Society of London. Series A: Mathematical, Physical and Engineering Sciences*, *362*(1824), 2477-2512.
- [12] Genovese, C., Ampelli, C., Perathoner, S., & Centi, G. J. J. o. c. (2013). Electrocatalytic conversion of CO₂ on carbon nanotube-based electrodes for producing solar fuels. *308*, 237-249.
- [13] Geus, J. W., van Dillen, A. J. . (2008). Preparation of supported catalysts by deposition-precipitation. *Handbook of Heterogeneous Catalysis: Online*, 428-467.
- [14] Geus, J. W. D. P. A. (1968). Dutch Patent Application 6705, 259, 1967. 236.
- [15] Griffin, G. L., & Bugayong, J. J. M. O. P. L. A. (2014). Electrochemical Reduction of CO₂ using Copper Oxide Nanoparticles supported on Glassy Carbon Electrodes. *1677*.
- [16] Guo, K., Gu, M., & Yu, Z. J. E. T. (2017). Carbon nanocatalysts for aquathermolysis of heavy crude oil: Insights into thiophene hydrodesulfurization. *5*(8), 1228-1234.
- [17] Han, Z., Kortlever, R., Chen, H.-Y., Peters, J. C., & Agapie, T. J. A. c. s. (2017). CO₂ reduction selective for C_{≥2} products on polycrystalline copper with N-substituted pyridinium additives. *3*(8), 853-859.
- [18] Hori, Y., Konishi, H., Futamura, T., Murata, A., Koga, O., Sakurai, H., & Oguma, K. (2005). "Deactivation of copper electrode" in electrochemical reduction of CO₂. *Electrochimica Acta*, *50*(27), 5354-5369. doi:10.1016/j.electacta.2005.03.015

- [19] Hori, Y., Murata, A., & Takahashi, R. J. J. o. t. C. S., *Faraday Transactions 1: Physical Chemistry in Condensed Phases*. (1989). Formation of hydrocarbons in the electrochemical reduction of carbon dioxide at a copper electrode in aqueous solution. 85(8), 2309-2326.
- [20] Hossain, S. S., & Ahmed, S. J. J. o. N. (2014). Electrochemical reduction of carbon dioxide over CNT-supported nanoscale copper electrocatalysts. *2014*, 9.
- [21] Jearl Walker, D. H., Robert Resnick. (2014). *Fundamentals of Physics* (10th ed.): John Wiley & Sons, Inc.
- [22] Jinli Qiao, Y. L., Jiujun Zhang. (2016). *Electrochemical Reduction of Carbon Dioxide, Fundamentals and Technologies*: Taylor & Francis Group.
- [23] Jitaru, M. (2007). Electrochemical carbon dioxide reduction - fundamental and applied topics, review *Journal of the University of Chemical Technology and Metallurgy*.
- [24] Kar, S., Kothandaraman, J., Goepfert, A., & Prakash, G. K. S. (2018). Advances in catalytic homogeneous hydrogenation of carbon dioxide to methanol. *Journal of CO₂ Utilization*, 23, 212-218. doi:10.1016/j.jcou.2017.10.023
- [25] Kuhl, K. (2013). *Electrochemical reduction of carbon dioxide on transition metal surfaces* (Doctor of philosophy), Stanford University, Retrieved from <http://purl.stanford.edu/ch356ht8074>
- [26] Kuhl, K. P., Hatsukade, T., Cave, E. R., Abram, D. N., Kibsgaard, J., & Jaramillo, T. F. J. J. o. t. A. C. S. (2014). Electrocatalytic conversion of carbon dioxide to methane and methanol on transition metal surfaces. *136*(40), 14107-14113.
- [27] Li, F., MacFarlane, D. R., & Zhang, J. (2018). Recent advances in the nanoengineering of electrocatalysts for CO₂ reduction. *Nanoscale*, 10(14), 6235-6260. doi:10.1039/C7NR09620H
- [28] Lion Specialty Chemicals Co., L. (2019). KETJENBLACK Highly Electro-Conductive Carbon Black. Retrieved from <https://www.lion-specialty-chem.co.jp/en/product/carbon/carbon01.htm>
- [29] Loiudice, A., Lobaccaro, P., Kamali, E. A., Thao, T., Huang, B. H., Ager, J. W., & Buonsanti, R. J. A. C. I. E. (2016). Tailoring copper nanocrystals towards C₂ products in electrochemical CO₂ reduction. *55*(19), 5789-5792.
- [30] Ma, S., Lan, Y., Perez, G. M., Moniri, S., & Kenis, P. J. J. C. (2014). Silver supported on titania as an active catalyst for electrochemical carbon dioxide reduction. *7*(3), 866-874.
- [31] Ma, T., Fan, Q., Tao, H., Han, Z., Jia, M., Gao, Y., Ma, W., & Sun, Z. (2017). Heterogeneous electrochemical CO₂ reduction using nonmetallic carbon-based catalysts: current status and future challenges. *Nanotechnology*, 28(47), 472001. doi:10.1088/1361-6528/aa8f6f
- [32] Malik, M. I., Malaibari, Z. O., Atieh, M., & Abussaud, B. J. C. E. S. (2016). Electrochemical reduction of CO₂ to methanol over MWCNTs impregnated with Cu₂O. *152*, 468-477.
- [33] Ohya, S., Kaneco, S., Katsumata, H., Suzuki, T., & Ohta, K. J. C. T. (2009). Electrochemical reduction of CO₂ in methanol with aid of CuO and Cu₂O. *148*(3-4), 329-334.
- [34] Pérez-Cadenas, A. F., Ros, C. H., Morales-Torres, S., Pérez-Cadenas, M., Kooyman, P. J., Moreno-Castilla, C., & Kapteijn, F. J. C. (2013). Metal-doped carbon xerogels for the electro-catalytic conversion of CO₂ to hydrocarbons. *56*, 324-331.
- [35] Peterson, A. A., Abild-Pedersen, F., Studt, F., Rossmeisl, J., Nørskov, J. K. J. E., & Science, E. (2010). How copper catalyzes the electroreduction of carbon dioxide into hydrocarbon fuels. *3*(9), 1311-1315.

- [36] Pigewh Isa Amos, H. L., Kayode Adesina Adegoke, Ededet Akpan Eno, Akakuru Ozioma Udochukwu, Thomas Odey Magub. (2018). Understanding the Mechanism of Electrochemical Reduction of CO₂ Using CuCu-Based Electrodes *Asian Journal of Nanoscience and Materials*.
- [37] Programme, U. N. E. (2019). Global Environment Outlook 6. Retrieved from <https://www.unenvironment.org/resources/global-environment-outlook-6>
- [38] Review, W. P. (2019). World Population. Retrieved from <http://worldpopulationreview.com>
- [39] Rogers, C., Perkins, W. S., Veber, G., Williams, T. E., Cloke, R. R., & Fischer, F. R. J. J. o. t. A. C. S. (2017). Synergistic enhancement of electrocatalytic CO₂ reduction with gold nanoparticles embedded in functional graphene nanoribbon composite electrodes. *139*(11), 4052-4061.
- [40] Ros, T. G., Van Dillen, A. J., Geus, J. W., & Koningsberger, D. C. (2002). Surface oxidation of carbon nanofibres. *Chemistry—A European Journal*, *8*(5), 1151-1162.
- [41] Savéant, J.-M. J. C. R. (2008). Molecular catalysis of electrochemical reactions. Mechanistic aspects. *108*(7), 2348-2378.
- [42] Scott, H. F. (2016). *Elements of chemical reaction engineering*: Prentice Hall.
- [43] Shenzhen Nanotech Port Co., L. (2019). Nanotubes.com.cn. Retrieved from http://nanotubes.com.cn/product_detail.aspx?ProductsID=48&CateID=37&ProductsCateID=37
- [44] Ud Din, I., Shaharun, M. S., Subbarao, D., & Naeem, A. (2014). *Homogeneous deposition precipitation method for synthesis of carbon nanofibre based Cu-ZrO₂ catalyst for hydrogenation of CO₂ to methanol*. Paper presented at the Applied Mechanics and Materials.
- [45] Wang, W.-H., Himeda, Y., Muckerman, J. T., Manbeck, G. F., & Fujita, E. J. C. r. (2015). CO₂ hydrogenation to formate and methanol as an alternative to photo-and electrochemical CO₂ reduction. *115*(23), 12936-12973.
- [46] Xi, W., Ma, R., Wang, H., Gao, Z., Zhang, W., & Zhao, Y. (2018). Ultrathin Ag Nanowires Electrode for Electrochemical Syngas Production from Carbon Dioxide. *ACS Sustainable Chemistry & Engineering*, *6*(6), 7687-7694.
- [47] Xie, H., Wang, T., Liang, J., Li, Q., & Sun, S. (2018). Cu-based nanocatalysts for electrochemical reduction of CO₂. *Nano Today*, *21*, 41-54. doi:10.1016/j.nantod.2018.05.001
- [48] Yamamoto, T., Tryk, D. A., Fujishima, A., & Ohata, H. J. E. a. (2002). Production of syngas plus oxygen from CO₂ in a gas-diffusion electrode-based electrolytic cell. *47*(20), 3327-3334.
- [49] Yao, P., Qiu, Y., Zhang, T., Su, P., Li, X., Zhang, H. J. A. S. C., & Engineering. (2019). N-Doped Nanoporous Carbon from Biomass as a Highly Efficient Electrocatalyst for the CO₂ Reduction Reaction. *7*(5), 5249-5255.
- [50] Yun, K.-S., Kim, B.-R., Kang, W.-S., Jung, S.-C., Myung, S.-T., & Kim, S.-J. (2013). Preparation of Carbon Blacks by Liquid Phase Plasma (LPP) Process. *Journal of Nanoscience and Nanotechnology*, *13*(11), 7381-7385. doi:10.1166/jnn.2013.7861
- [51] Zhu, X., Gupta, K., Bersani, M., Darr, J. A., Shearing, P. R., & Brett, D. J. J. E. A. (2018). Electrochemical reduction of carbon dioxide on copper-based nanocatalysts using the rotating ring-disc electrode. *283*, 1037-1044.
- [52] Zielke, U., Hüttinger, K., & Hoffman, W. J. C. (1996). Surface-oxidized carbon fibers: I. Surface structure and chemistry. *34*(8), 983-998.
- [53] Zoski, C. G. (2006). *Handbook of electrochemistry*: Elsevier.

Appendix A

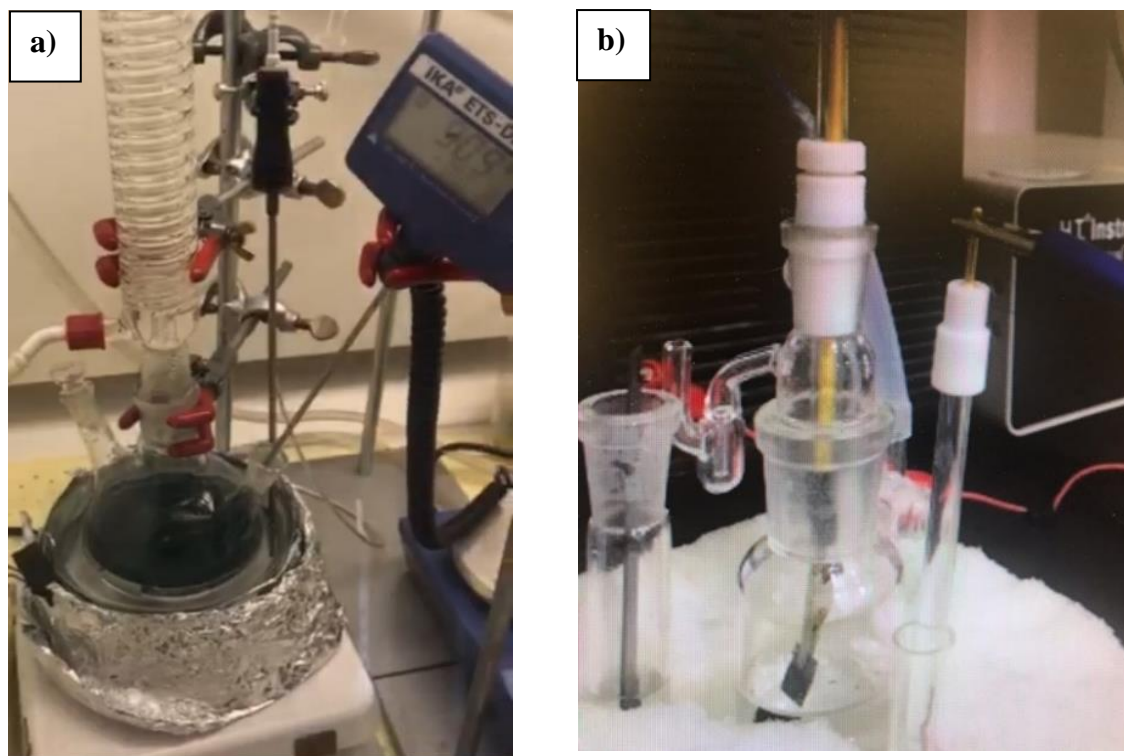


Figure A1. a) Image of the experimental setup during colloidal deposition precipitation procedures, b) image of the three-electrode cell for CV tests.

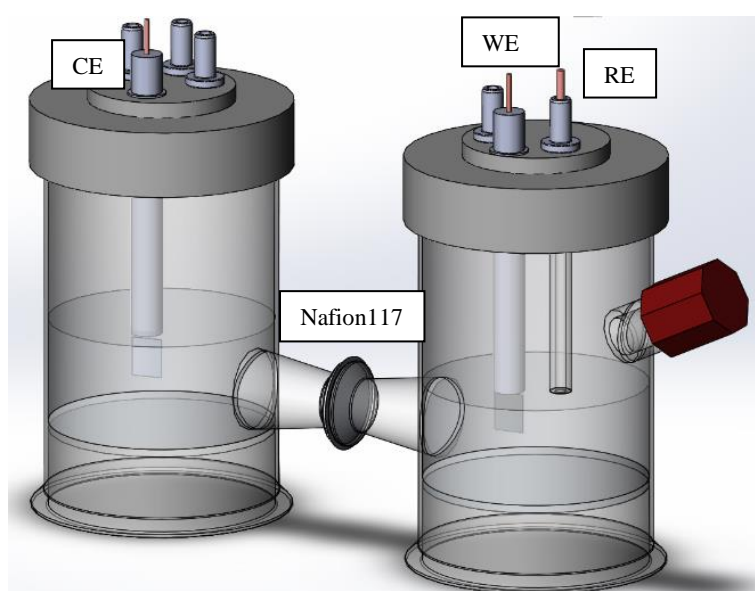


Figure A2. Illustration of H-type electrochemical cell used for chronoamperometry measurements.

Appendix B

The water peak is very prominent even after suppression assigned to 4.8 δ ppm chemical shift. The internal standard, DMSO, appears at 2.68 δ ppm, HCOOH assigned to 8.35 δ ppm and CH₃OH to 3.34 δ ppm [17]. Quantification of electrolysis products achieved via linear normalisation performed by two independent tests of known concentrations.

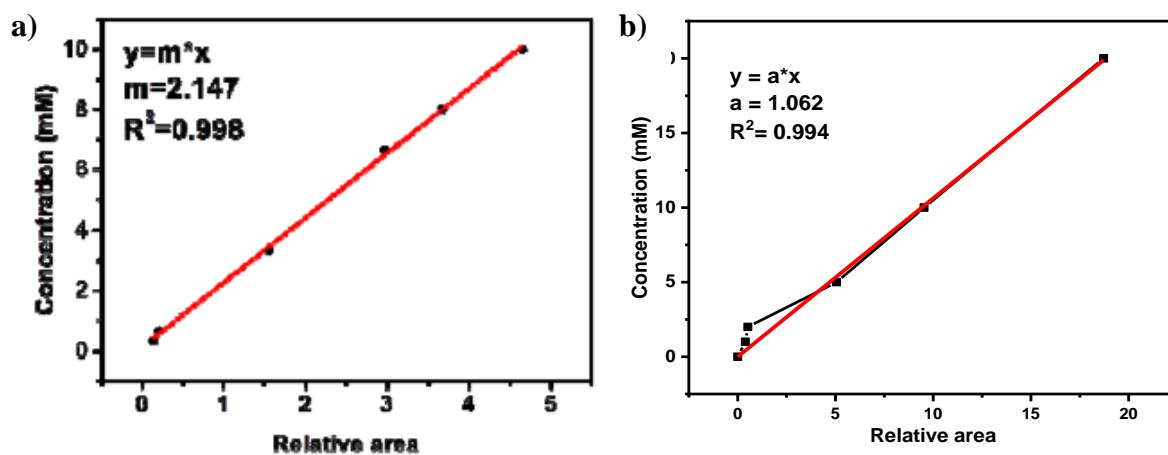


Figure B1. Linear relationship between reactants' concentrations and relative area of associated chemical shift against DMSO concentration of: a) HCOOH [46], b) CH₃OH.